AGU PUBLICATIONS

JGR

Journal of Geophysical Research: Solid Earth

RESEARCH ARTICLE

10.1002/2014JB011591

Key Points:
- We analyze multicomponent seismic data acquired on the Whillans Ice Stream
- The analysis reveals that the ice mass below the firn is VTI
- We derive the average temperature and mean COF properties of the ice column

Correspondence to:
S. Picotti,
spicotti@ogs.trieste.it

Citation:
Picotti, S., A. Vuan, J. M. Carcione, H. J. Horgan, and S. Anandakrishnan (2015), Anisotropy and crystalline fabric of Whillans Ice Stream (West Antarctica) inferred from multicomponent seismic data, *J. Geophys. Res. Solid Earth*, *120*, doi:10.1002/2014JB011591.

Received 15 SEP 2014
Accepted 20 APR 2015
Accepted article online 24 APR 2015

Anisotropy and crystalline fabric of Whillans Ice Stream (West Antarctica) inferred from multicomponent seismic data

Stefano Picotti[1], Alessandro Vuan[1], José M. Carcione[1], Huw J. Horgan[2], and Sridhar Anandakrishnan[3]

[1] Istituto Nazionale di Oceanografia e di Geofisica Sperimentale (OGS), Sgonico, Trieste, Italy, [2] Antarctic Research Centre, Victoria University of Wellington, Kelburn Pde, ACC Wellington, New Zealand, [3] Department of Geosciences, Earth and Environmental Systems Institute, Pennsylvania State University, University Park, Pennsylvania, USA

Abstract Crystal orientation fabric (COF) describes the intrinsic anisotropic nature of ice and is an important parameter for modeling glacier flow. We present the results of three-component active-source seismic observations from the Whillans Ice Stream (WIS), a fast-flowing ice stream in West Antarctica. Surface-wave dispersion analysis, ray tracing, and traveltime inversion of compressional (*P*) and shear (*S*) waves reveal the presence of transversely isotropic ice with a vertical axis of symmetry (VTI) beneath approximately 65 m of isotropic firn. The ice stream is characterized by weak anisotropy, involving an average ice thickness of approximately 780 m. The analysis indicates that about 95% of the ice mass is anisotropic, and the crystalline *c* axes span within an average broad cone angle of 73 ± 10° with respect to the vertical axis. Moreover, the mean temperature *T* (below the firn) estimated from seismic data is −15 ± 5°C. These data do not show evidence of englacial seismic reflectivity, which indicates the lack of abrupt changes in the COF. The presence of azimuthal anisotropy due to transversely compressive flow or fractures aligned along a preferential direction is also excluded. We suggest that the observed VTI ice structure is typical of large ice streams in regions where basal sliding and bed deformation dominate over internal glacial deformation.

1. Introduction

The preferential alignment of ice crystals within ice masses induces intrinsic anisotropy, which is observed in ice cores [*Gow and Williamson*, 1976; *Thorsteinsson et al.*, 1997], and can be remotely sensed using geophysical methods [*Bentley*, 1971; *Blankenship and Bentley*, 1987; *Matsuoka et al.*, 2003]. Crystal orientation fabric (COF) describes the internal structure of ice, where crystal orientations are commonly characterized by the distribution of *c* axes (the symmetry axes of the ice crystals) plotted on a lower hemisphere Schmidt projection [*Thorsteinsson et al.*, 1997]. Hexagonal ice exhibits a highly anisotropic rheology, where shear deformations parallel to the basal plane are orders of magnitude easier to achieve than perpendicular to it [*Hobbs*, 1974]. COF observations of ice sheets are sparse and typically consist of measurements of thin sections of ice cores concentrated close to the major ice domes and ice divides [e.g., *Gow et al.*, 1997; *Gow and Meese*, 2007; *Durand et al.*, 2009; *Pettit et al.*, 2007, 2011]. The distribution of *c* axes observed in ice cores is nearly random in the near surface [*Gow et al.*, 1997; *Thorsteinsson et al.*, 1997]. With increasing depth, vertical compression and/or simple shear induce the *c* axes to rotate and cause their distribution to gradually tighten into a cone pattern [e.g., *Gow and Williamson*, 1976]. An often observed feature, in particular close to ice domes and ice divides, is a gradual rotation of the *c* axes toward the vertical with depth. This preferential alignment of ice crystals generates anisotropy, whose general trend is to increase with depth. Close to the bed, a distributed fabric is generally observed and is thought to result from the dominance of dynamic migration recrystallization [e.g., *Alley et al.*, 1986a, 1986b; *Diprinzio et al.*, 2005]. Flowing away from ice domes and ice divides, internal deformations occur in the ice mass, leading to evolution of the crystal fabric. *Alley* [1988] showed that in ice sheets where normal stress dominate and the flow is longitudinally extensional and vertically compressional, basal shear, parallel (neutral) flow, and divergent flow cause *c* axes to rotate toward the vertical axis. The rotation is independent of azimuth in transversely divergent flow. Moreover, neutral flow causes a transverse elongation of the distribution, whereas convergent flow causes *c* axes to rotate toward a vertical plane transverse to flow. The evolution of the COF during deformation has been reproduced in laboratory studies [e.g., *Bouchez and Duval*, 1982; *Budd and Jacka*, 1989; *Wilson et al.*, 2003], confirming theoretical findings [*Alley*, 1988; *van der Veen and Whillans*, 1994].

Currently, less is known about the COF from peripheral ice sheets and fast-flowing ice streams. There are few ice core observations away from the main ice domes and ice divides (e.g., Law Dome, East Antarctica [*Russell-Head and Budd*, 1979; *Budd and Jacka*, 1989], Byrd, West Antarctica [*Gow and Williamson*, 1976], Dye 3, Greenland [*Herron et al.*, 1982; *Dahl-Jensen and Gundestrup*, 1987], and Barnes Ice Cap, Baffin Island [*Hooke*, 1973]). However, many radio-echo sounding (RES) and active-source seismic observations around Antarctica and Greenland have revealed layered regions of anisotropy and great spatial complexity [e.g., *Matsuoka et al.*, 2003; *Horgan et al.*, 2008, 2011] that cannot be observed in ice cores, because borehole-based techniques can provide only local information. Knowledge of the extent and distribution of anisotropy in ice sheets can be used to constrain models that account for anisotropy [e.g., *Pettit et al.*, 2007] or validate those that predict fabric evolution [e.g., *Martín et al.*, 2009].

Ice COF can be measured using geophysical, core- and borehole-based methods, namely, RES, ultrasonic methods, and surface-based active-source seismics. Since the 1960s, RES has represented one of the main investigation tools in glaciology with which to assess the subsurface properties of polar ice sheets, ice caps, and glaciers. Several investigations [e.g., *Woodruff and Doake*, 1979; *Matsuoka et al.*, 2009] have noted that the polarization of radar waves transmitted through ice sheets is significantly changed in the returned echoes. This change indicates that ice COF induces the birefringence effect, which can thus be analyzed to infer ice COF properties [*Matsuoka et al.*, 2003]. Surface seismic methods and ultrasonic methods infer COF properties by exploiting the anisotropy of ice. The basic phenomenon is that the velocity of the elastic waves along the *c* axis is different from the velocity in the orthogonal direction [*Bennett*, 1968; *Röthlisberger*, 1972]. Ultrasonic methods have been used for direct COF measurements in ice cores. Using both compressional (*P*) and shear (*S*) waves, *Anandakrishnan et al.* [1994], logged the upper 2250 m of the Greenland Ice Sheet Project II (GISP2) core and showed a progressive clustering of COFs versus depth. In particular, shear waves revealed a slight degree of obliquity in the COF cone clustering that increases with depth, indicating that deformation is not symmetric around the vertical direction. Recently, *Gusmeroli et al.* [2012] estimated COF properties continuously with depth using sonic-log measurements from the Dome C (East Antarctica) borehole, defining a relation for *P* and vertically polarized (*SV*) shear wave velocities. Surface-based seismic methods have a lower resolution than ultrasonic methods. However, the former methods are useful in inferring the average COF properties and mean temperature of ice sheets and ice streams. *Bentley* [1971] used reflected *P* waves, converted *P* to *S* reflections, and *P* and *S* refracted arrivals to infer COF parameters from the degree of anisotropy at many different sites in West Antarctica. He showed that, away from the ice divides, *c* axes are often oriented in the direction of flow and suggested a proportionality between the inclination of COF cones and the longitudinal strain rate. *Kohnen* [1974] used several seismic velocity measurements from Greenland and Antarctica to determine the empirical relation between seismic velocities and temperatures in isotropic ice. *Blankenship and Bentley* [1987] used *P* waves reflected at wide angles from the bedrock near Dome C to build a vertical transverse isotropic (VTI) model of the ice sheet, from which they inferred both the average temperature and mean COF properties of the entire ice column. The VTI structure is a particular distribution of COF, where the symmetry of the ice fabric is vertically oriented because the ice crystal *c* axes are evenly distributed within a vertical cone pattern.

Shear waves have been used to characterize the properties and structure of polar ice sheets and the underlying sediments [e.g., *Blankenship et al.*, 1986; *Anandakrishnan and Bentley*, 1993]. Because the degree of anisotropy of *S* waves in ice is comparable of that of *P* waves [*Gusmeroli et al.*, 2012; *Anandakrishnan et al.*, 1994], *S* waves can be useful to better constrain the COF models in regions of the ice sheet where seismic anisotropy has been observed. An interesting phenomenon involving *S* waves is shear wave splitting, which is an effect similar to birefringence in optics and occurs whenever a shear wave travels through an anisotropic material [*Crampin*, 1994, 2011; *Savage*, 1999]. Basically, the incident wave is split into two waves polarized along mutual perpendicular directions and propagating with different velocities. The measured delay time between the two split waves depends on the degree of anisotropy and on the thickness of the anisotropic layer considered. A few works used *S* waves to study the seismic anisotropy in ice by exploiting shear wave splitting. For example, *Anandakrishnan* [1999] analyzed the high-frequency events originating from basal microearthquakes in ice stream C (Siple Coast, West Antarctica), reporting a strong polarization of the *S* wave arrivals into longitudinal and transverse components. The resulting shear wave splitting revealed a significant anisotropic fabric in the ice stream, and the weak azimuthal dependence in the delay time suggested a vertical symmetry axis for the fabric.

Over the last 20 years, active and passive surface wave methods have been applied in engineering seismology to define the local seismic response and in geotechnics to enable the seismic characterization of soft soils. Surface waves are useful in seismic anisotropy investigations, for two reasons. First, they carry more than two thirds of the total generated seismic energy [*Richart et al.*, 1970] and thus have a high signal/noise ratio. Second, they are sensitive to azimuthal anisotropy because shear wave splitting induces dispersion splitting of surface waves [*Zhang et al.*, 2009]. The application of surface wave methods to characterize ice properties is still very limited. *Acharya and Bentley* [1978] attempted to model the observed surface wave dispersion in Marie Byrd Land (Antarctica) by using a finite difference method. Active-source seismic experiments were conducted on the Jakobshavn Glacier (Greenland) to evaluate the potential utility of surface wave methods on glaciers [*Tsoflias et al.*, 2008] and on the Erebus Ice Shelf (Antarctica) to characterize the near-surface polar firn [*Armstrong*, 2009]. Preliminary results demonstrated that surface wave methods can provide the shear wave velocities of the subsurface, which may allow for a better understanding of firn and ice mechanical properties.

In this work we infer the anisotropic and COF properties of the Whillans Ice Stream (WIS) using the three-component seismic data recorded on the Subglacial Lake Whillans (SLW) during the active-source experiment described in *Horgan et al.* [2012]. We analyze diving waves, surface waves, and *P*, *SV*, converted *P-SV* and *SH* waves reflected from the bed, to determine the origin and character of the ice stream anisotropy. This information is critical for efforts to extract fabric properties from seismic anisotropy, because when observed from the surface, the intrinsic anisotropy of the deep ice may be affected by different distortions that should be considered. For example, the possible presence of deviatoric stresses and fractures aligned along preferential directions, potentially produced by the ice flow, can modify the orientation of the symmetry axis inducing azimuthal anisotropy. Similarly, the presence of internal layering, often reported by georadar data [*Fujita et al.*, 1999; *Matsuoka et al.*, 2003; *Christianson et al.*, 2012], may induce other anisotropic effects [*Backus*, 1962; *Carcione*, 2015; *Picotti et al.*, 2010, 2012] due to the texture of the ice mass. All of these effects should be excluded from the seismic data before evaluating the COF properties.

First, we describe the study site, acquired data and analytical methods employed, namely, surface wave dispersion analysis, ray tracing, and traveltime inversion of *P* and *S* waves. Two anisotropic velocity models are presented here: the first model, referred to as the VTI model, is based on the fundamental elastic constants [*Carcione*, 2015; *Picotti et al.*, 2010, 2012] and the second model, referred to as the COF model, is based on the fabric properties of the ice [*Bennett*, 1968; *Blankenship and Bentley*, 1987]. A review of the propagation properties of elastic waves through VTI media and of the COF properties of polar ice is included. Second, we describe the application of the methods to extract the velocities from the seismic data and verify whether the medium is effectively VTI. Finally, we compare the two models and compute the average temperature and fabric properties of the entire ice column at the SLW location by fitting the energy (group) velocities of the body waves reflected from the bed. We also determine the fabric properties in discrete depth ranges down to a depth of 200 m using the results of the surface wave analysis.

2. The Study Site

The WIS, previously known as Ice Stream B, forms one of the main drainage conduits of ice from the interior of West Antarctica that feeds the Ross Ice Shelf (Figure 1a). This ice stream flows at over 300 m a^{-1}, although its driving stresses are lower than 20 kPa [*Bentley*, 1987; *Beem et al.*, 2010]. The flow is not continuous, but characterized by a stick-slip motion, in which long periods of relative quiescence have been followed by short, typically diurnal, bursts [*Bindschadler et al.*, 2003; *Winberry et al.*, 2009]. In recent decades, the periods of quiescence have been growing longer, suggesting the possibility of a future stagnation [*Joughin et al.*, 2002, 2005; *Winberry et al.*, 2014]. Using surface elevation observations from the Geoscience Laser Altimeter System aboard the Ice Cloud and land Elevation Satellite (ICESat), *Fricker et al.* [2007] and *Fricker and Scambos* [2009] provided evidence for the presence of a subglacial lake system beneath the WIS. Recent seismic and RES surface observations [*Horgan et al.*, 2012; *Christianson et al.*, 2012] confirmed the presence of a shallow active water reservoir beneath the WIS, called Subglacial Lake Whillans (SLW), whose location is shown in Figure 1a. These works also show that the major part of the bed appears wet around the SLW, with meters-thick soft sediments or thin water lenses. Other evidence of the presence of highly deformable till and water beneath the WIS was provided by active [*Blankenship et al.*, 1986, 1987] and passive [*Anandakrishnan and Bentley*, 1993] seismic experiments, by glaciological drilling and instrumentation in the late 1980s and 1990s [*Engelhardt and Kamb*, 1997, 1998; *Kamb*, 2001], and by recent drilling operations [*Tulaczyk et al.*, 2014], which definitively confirmed the existence of the

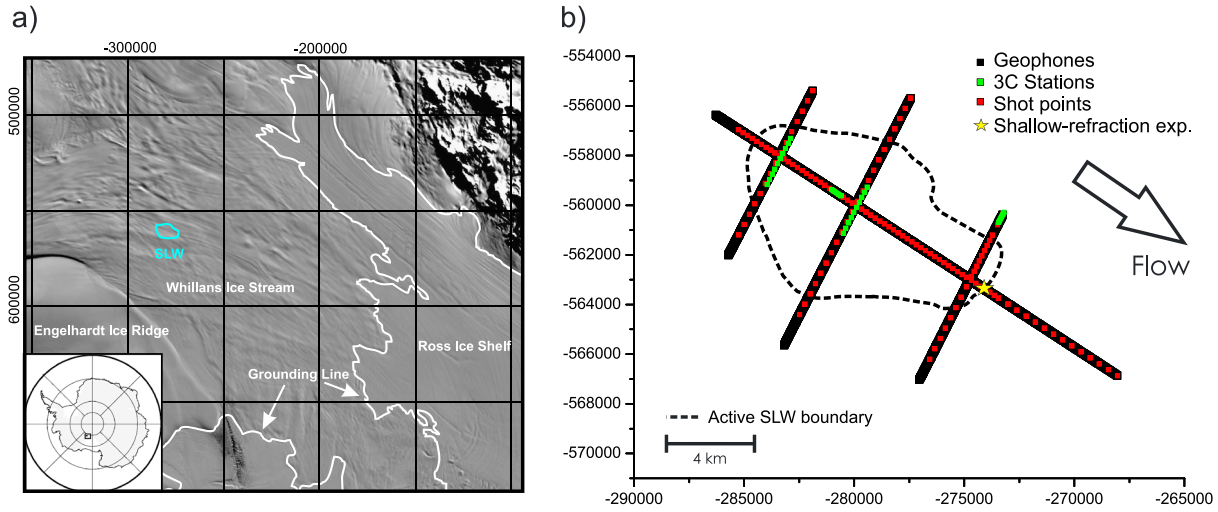

Figure 1. (a) Satellite map showing the location of SLW (adapted from *Horgan et al.* [2012]) and (b) the survey profiles. Polar stereographic projection with true scale at −71°. The background imagery and grounding line in Figure 1a are from Moderate Resolution Imaging Spectroradiometer Mosaic of Antarctica [*Horgan et al.*, 2012].

SLW. *Tulaczyk et al.* [2014] also confirmed the ice thicknesses estimated from the surface seismic and RES surveys [*Horgan et al.*, 2012; *Christianson et al.*, 2012]. The above experimental findings imply that the subglacial sediments below the WIS are extremely weak, and the principal component of the ice stream movement is basal sliding or deformation in the basal sediment layer, rather than deformation in the ice. However, *Tulaczyk et al.* [2000] demonstrated that ice streams are subject to thermally triggered instabilities, and small perturbations in the basal thermal energy balance may lead to rapid changes in the basal conditions that determine the ice streaming regime.

3. Seismic Data Acquisition

In the austral summer of 2010–2011, a comprehensive surface geophysics program surveyed a location on the WIS. The main target of the survey [*Horgan et al.*, 2012; *Christianson et al.*, 2012] was the seismic and radar characterization of the SLW (Figure 1a), an active subglacial lake that is the subject of an ongoing WISSARD subglacial access program [*Fricker et al.*, 2011]. Four active-source seismic profiles were acquired during this survey: one profile parallel to the ice stream flow direction following the long axis of the lake (referred to as the longitudinal profile) and three transverse profiles across the lake (Figure 1b).

Two types of surveys were undertaken, using a Geometrics GEODE seismic system: one to obtain the characteristics of the firn and another to define the anisotropy of the deeper ice. Moreover, newly acquired GPS observations were combined with surface elevation observations from the ICESat, as described in *Horgan et al.* [2012] and *Christianson et al.* [2012]. To analyze the velocity profile within the firn, a shallow-refraction data set was generated using stacked hammer blows onto a wooden surface embedded in the snow. This experiment, referred to as the hammer shallow-refraction experiment, is located on the longitudinal profile, as shown in Figure 1b. The data were recorded on a 24-channel seismic system using georods spaced 20 m apart and consisting of five 40 Hz geophones wired in series [*Voigt et al.*, 2013]. The digital sample interval was 0.25 ms, and the maximum offset was 470 m, which is sufficiently large to define the velocity profile of the entire firn layer. To acquire the three components of the ground motion, the georods were rotated through the three mutually perpendicular axes. In each profile of this work, the horizontal longitudinal and transverse components are parallel and orthogonal to the profile, respectively. During this survey, the offset between the source position and the first georod varied from 1 m to 10 m. Thus, we combined the traces from different shots into a single-shot ensemble with irregular trace spacing. The spacing was increased with increasing offset to gain better resolution in the shallow part of the firn, which exhibits the strongest velocity gradient. The obtained composite ensembles are shown in Figure 2, where the *P* and *S* diving-wave first breaks to pick for traveltime inversion are indicated.

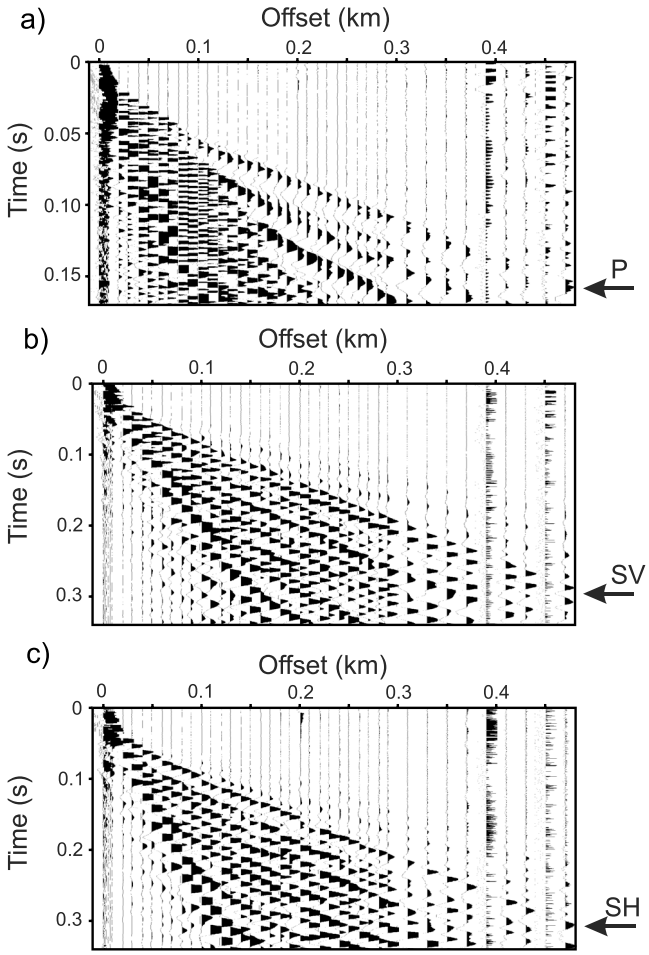

Figure 2. Hammer shallow-refraction seismograms as recorded by the georods along the longitudinal profile. (a) The vertical component. (b) The horizontal longitudinal and (c) transverse components. To acquire the three components, the georods were rotated through the three mutually perpendicular axes. The *P*, *SV*, and *SH* diving-wave first breaks are indicated. These seismograms are obtained by combining the traces from different shot gathers to obtain a shot ensemble with irregular trace spacing.

All the other data, aimed at defining the anisotropy of the deeper ice, were generated using 0.4 kg PETN (pentaerythritol tetranitrate) charges buried at 27 m depth using a hot-water drill. The data were recorded on a 48-channel seismic system, and the sensors consisted of alternating 28 Hz single vertical (1C) geophones and georods spaced 20 m apart. Moreover, multicomponent data were acquired using 10 continuously recording three-component (3C) stations. The 3C stations were first placed along the longitudinal profile, spaced 24 m apart and then moved to the transverse profiles, where the spacing was 24 m and 240 m (Figure 1b). Each of these stations consisted of a Guralp 40-T broadband seismometer with a 40 s corner period, coupled to a Reftek RT-130 data acquisition system equipped with GPS timing. The maximum offset was 4320 m for the data recorded using the 3C stations and 1910 m for the other data. Figure 3 shows the vertical and horizontal (longitudinal and transverse) components recorded by the 3C stations along the longitudinal profile used for the surface wave analysis. To enhance the signals of the surface waves, a 2–20 Hz band-pass filter was applied. These ensembles were obtained by combining a large number of shots and sorting the traces by offset. This procedure was necessary because only 10 3C stations were used throughout the survey. For the surface wave analysis, we use Rayleigh (marked A) and Love (marked B) waves (Figure 3). Some noise in these data is visible (marked D) due to ice falls in crevasses after the shots.

Theoretically, an explosive point source in a perfectly isotropic homogeneous medium generates only *P* waves [*Stevens et al.*, 2008]. However, in a real medium, *S* waves can be indirectly generated by scattering and mode conversion. Moreover, the detonation of an explosive charge is not perfectly spherical, and asymmetries are always present in the medium surrounding the source cavity, enabling explosions to directly generate *S* waves [*Heelan*, 1953a, 1953b; *Geyer and Martner*, 1969; *Abo-Zena*, 1977]. In particular, the generation of both *P* and *S* waves from buried explosive charges in polar firn is frequently observed and has been well documented in the literature [*Blankenship et al.*, 1986; *King and Jarvis*, 2007]. In this experiment, the *P* waves reflected from the ice bottom interface were detected in the vertical component of both the standard geophones and the 3C stations. Similarly, the *SV* and *SH* waves were detected by the 3C stations in the horizontal longitudinal and transverse components, respectively. Figure 4 shows the (a) vertical, (b) horizontal longitudinal, and (c) transverse components recorded along the longitudinal and one of the transverse profiles. These ensembles are filtered with a 10–400 Hz band-pass filter to remove the surface waves and enhance the reflected events.

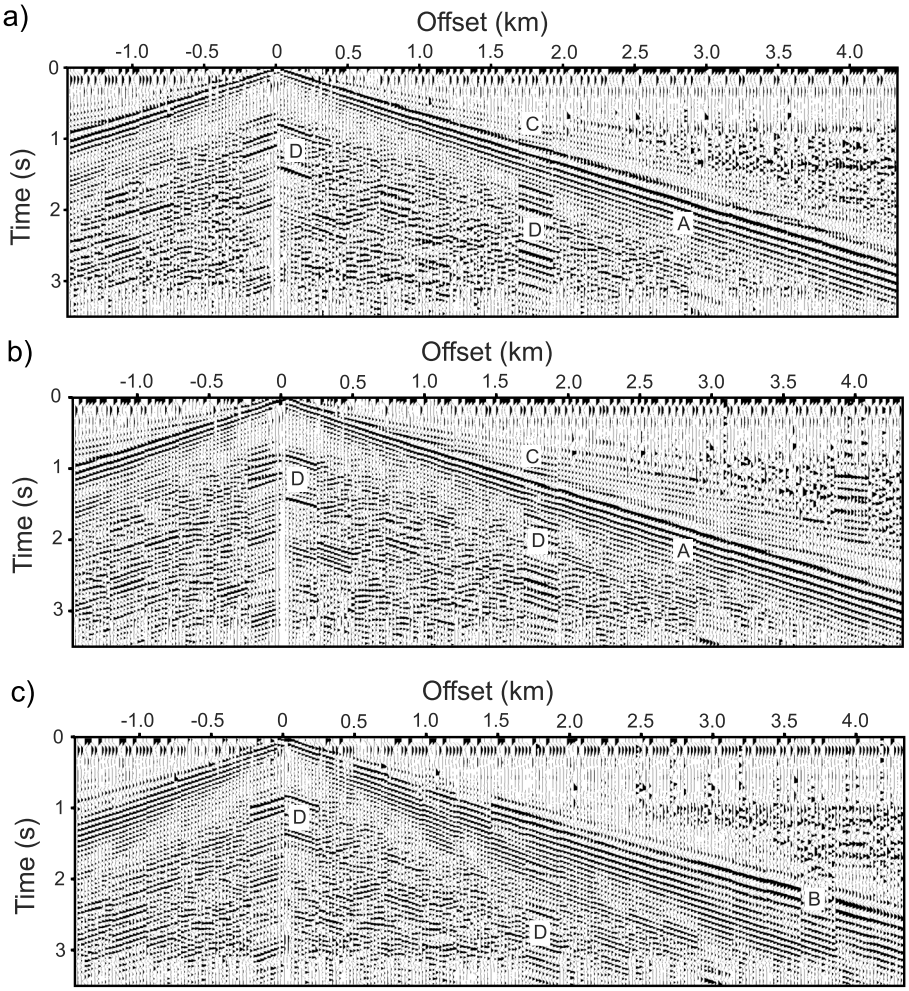

Figure 3. (a) Vertical, (b) horizontal longitudinal, and (c) transverse components recorded by the 3C stations placed along the longitudinal profile. A 2–20 Hz band-pass filter is applied to enhance the surface waves. The following main events are indicated: Rayleigh waves (A), Love waves (B), residual (after filtering) diving and multiple-diving waves in the firn (C) and seismic events due to ice falls in the crevasses after the shots (D). These seismograms are obtained by joining many different shot gathers.

4. Analytical Methods

The adopted methods expand on those employed in a previous work by *Blankenship and Bentley* [1987] at Dome C (East Antarctica). In this work, we use different analytical techniques for the different components of the seismic wavefield to determine the anisotropic characteristics of the ice mass at SLW location and to infer the mean temperature and average fabric properties of the entire ice column from the degree of anisotropy. In particular, the traveltime inversion of *P* and *S* diving waves in the firn allows us to determine the vertical velocity gradient down to approximately 65 m depth, whereas using the surface wave analysis we determine the anisotropic and COF characteristics over discrete depth ranges down to 200 m depth. Below the firn, a forward ray tracing minimizing method using *P*, *SV*, converted *P-SV* and *SH* waves reflected from the bed enables us to infer the average anisotropic velocity character, and hence the mean temperature and COF properties, of the entire ice column.

4.1. Traveltime Inversion of Diving Waves

Seismic investigations of ice sheet anisotropy and ice COF properties in polar regions are subject to a complication arising from raypath bending that occurs when the incident and reflected rays traverse the firn layer. To overcome this difficulty, the velocity-depth structure of the firn must first be determined for both *P* and *S* waves.

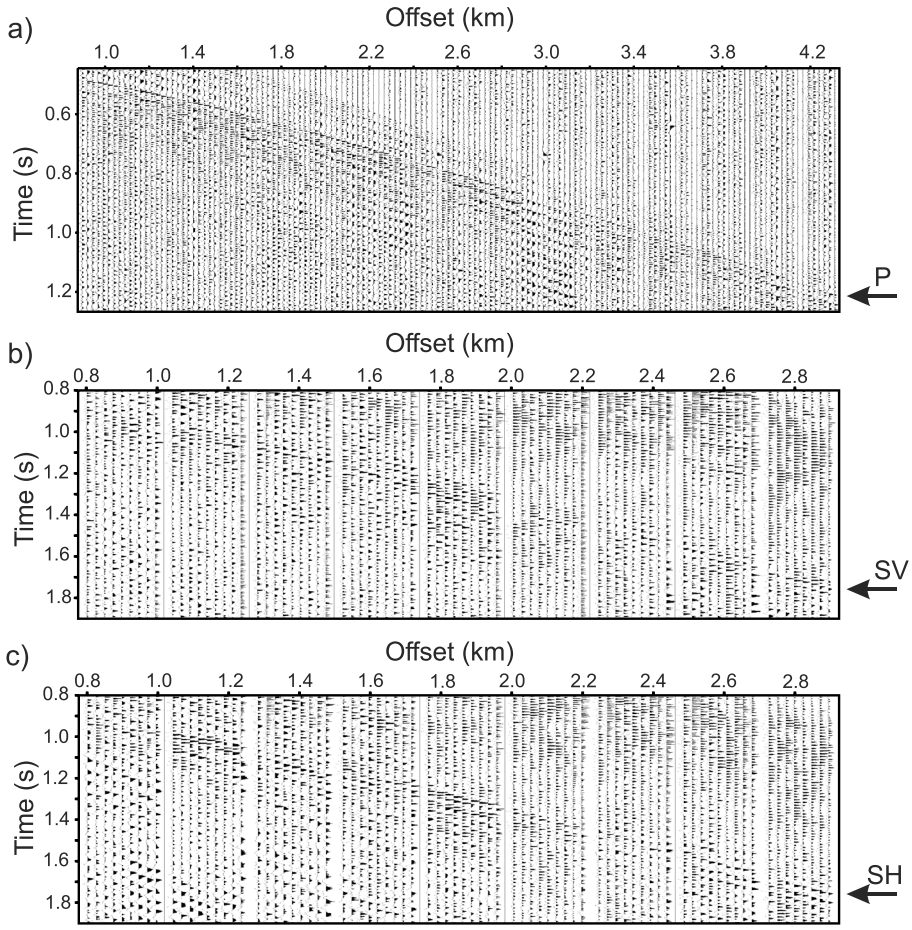

Figure 4. (a) Reflected *P* waves from the bed recorded on the vertical component by the 3C stations placed along the longitudinal profile. Reflected (b) *SV* and (c) *SH* waves from the bed recorded by the 3C stations placed along one of the transverse profiles, on the horizontal longitudinal and transverse components, respectively. A 10–400 Hz band-pass filter is applied to remove the surface waves. These ensembles are obtained by joining many different shot gathers.

The shallow part of polar ice sheets is subjected to snow densification, a metamorphic process activated by the pressure gradient due to the accumulation of snow and by the temperature gradient at the near surface [*Wilkinson*, 1988]. The density of firn increases continuously from the surface to the pore close-off depth, where the material can be considered glacial ice [*Herron and Langway*, 1980]. The compression of englacial bubbles below this depth increases the density until the maximum density of ice is reached. Because of this density structure, polar firn is generally laterally homogeneous with the seismic velocity continuously, but nonlinearly, increasing with depth. This velocity profile results in a continuous refraction of seismic waves. Due to this refraction, a ray leaving the source with a given take-off angle bends away from the vertical until the depth of maximum penetration, where the wave is traveling in a direction parallel to the surface (i.e., nearly horizontally if the surface slope is very low). Beyond this point, the wave continues to refract and the ray bends upward toward the surface [*Greenhalgh and King*, 1981]. These continuously refracted waves are also called diving waves and can effectively be used to resolve the firn velocity-depth structure by picking and inverting the first arrival traveltimes.

Because of its significant velocity gradient, polar firn represents a typical situation in which homogeneous layered models are inaccurate due to their dependence on the number of layers. In these cases, a mathematical idealization of curved raypaths enables a more reliable interpretation of traveltimes as a function of distance, provided that the velocity profile is monotonically increasing with depth [*Greenhalgh and King*, 1981]. The assumption of a monotonic increase in density and velocity with depth is not accurate at small scales because there can be high-density layers in the shallow snow pack [*Hörhold et al.*, 2011]. However, these

high-density layers, with dimensions of a few centimeters, are considerably smaller than the seismic wavelength, which is on the order of meters. Therefore, this assumption is acceptable at the scale of interest.

In this work, the traveltime inversion of first arrivals follows the method of Herglotz and Wiechert [*Herglotz*, 1907; *Wiechert*, 1910; *Nowack*, 1990], applied for the first time to data from Antarctica by *Kirchner and Bentley* [1979]. This inversion method calculates the velocity-depth function from traveltime-offset pairs of diving waves and is well suited to situations where the velocity increases monotonically with depth. For a diving wave, the ray parameter p is constant along the ray, such that

$$p = \frac{\sin\alpha_0}{v_0} = \frac{\sin\alpha}{v} = \frac{\sin\alpha_h}{v_h} = \frac{1}{v_h} = \text{constant}, \tag{1}$$

where v_0 is the initial velocity, v_h is the velocity at the deepest point h, and α_0, α, and $\alpha_h = 90°$ are the initial, intermediate, and final ray directions, respectively. Using the picked offset-traveltime pairs, the apparent velocity $v(x)$ can be determined by the reciprocal slope of the time-distance curve. If the velocity profile $v(z)$ increases smoothly with depth, the apparent velocity $v(x)$ will also increase smoothly with offset x. By interpolating the traveltimes of the picked diving-wave first breaks with a smoothing function, it is possible to derive the velocity $v(x)$ by taking the derivative of the traveltime with respect to the offset. Next, given a velocity $v_1 = v(z)$, the corresponding maximum penetration depth z of this velocity has to be determined, using the ray parameter expressed as $p = p(x)$. The inversion formula was introduced by Herglotz, Wiechet, and Bateman in 1910 [*Nowack*, 1990]. They found the following integral:

$$z(v_1) = \frac{1}{\pi}\int_0^{x(p_1)} \ln(\kappa + \sqrt{\kappa^2 - 1})\mathrm{d}x, \tag{2}$$

where $\kappa = p(x)/p_1$, $p_1 = 1/v_1$, and $x(p_1)$ is the maximum horizontal offset.

4.2. *S* Wave Velocity Profiling From Surface Waves

Surface wave dispersion analysis represents a valuable tool with which to assess *SV* and *SH* wave velocities versus depth. In fact, Rayleigh and Love surface waves, often generated during seismic reflection and refraction surveys, contain important information about the physical properties (mainly the *S* wave velocities) of the medium through which they propagate. In this work, surface waves are used to assess the *S* wave velocities of the firn and the underlying ice and to evaluate the ice anisotropy by separately inverting Rayleigh and Love wave phase velocities. The Rayleigh wave velocity depends mainly on the *SV* wave velocity, the *P* wave velocity and the density. The Love wave velocity depends mainly on the *SH* wave velocity and the density. The sensitivity of surface waves is related to the wavelength: the longer the wavelength, the deeper the wave can sample the subsurface. The sensitivity curves are the Fréchet derivatives of the velocity of the fundamental surface wave modes with respect to the *S* wave velocity at different depths [e.g., *Aki and Richards*, 2002], from which it is possible to infer the resolution versus depth of the dispersion curves. In the case of polar ice streams, high-frequency (f >10 Hz) Rayleigh and Love waves sample the shallow firn, whereas lower frequencies are expected to sample the underlying ice down to a depth of approximately 200–300 m. The theory behind the equations relating Rayleigh and Love waves to *SV* and *SH* waves has been described in many books and papers [e.g., *Lay and Wallace*, 1995; *Aki and Richards*, 2002].

The presence of azimuthal seismic anisotropy within an ice stream at shallow depths may be evaluated by comparing Rayleigh and Love wave velocities observed on orthogonal seismic surveys. This analysis also enables us to partition the anisotropic characteristics into discrete depth ranges. For the surface wave dispersion analysis we need to pick the Rayleigh and Love wave fundamental and higher modes. We enhance the detection and separation of the surface wave velocities by using a two-dimensional data transformation following *Herrmann* [2013] and *McMechan and Yedlin* [1981]. The phase velocity dispersion curves are obtained from a slant stack of the seismic traces followed by a transformation into the $\omega - p$ domain [*McMechan and Yedlin*, 1981], where ω and p denote, respectively, the angular frequency and the ray parameter associated with the surface waves. The interpretation of modal identity, often difficult where higher modes dominate and/or contaminate the data from regions of complex structure, is simple here because it is driven by seismic velocity models for ice [e.g., *Kohnen and Bentley*, 1973]. This behavior is due to the particular structure of polar ice sheets, which is characterized by *P* and *S* wave velocities and density that increase continuously with depth, showing steep gradients near the surface. Recorded waveforms from active-source experiments in this type of media generally exhibit a well-developed fan of surface waves (e.g., Figure 3) that can propagate efficiently across large distances.

S wave velocity profiling from surface wave dispersion curves is a nonlinear inversion problem. Numerous published papers have examined the surface wave inversion problem using global or heuristic algorithms [e.g., *Beaty et al.*, 2002; *Wathelet et al.*, 2004; *Yamanaka*, 2005]. Global method solutions typically require large computational efforts because they are based on genetic or Monte Carlo algorithms. An alternative approach is the linearized inversion, which has been extensively applied using least squares methods [e.g., *Wiggins*, 1972; *Nolet*, 1981; *Gabriels et al.*, 1987; *Xia et al.*, 1999; *Herrmann*, 2013]. *Luke and Calderon-Macías* [2007] showed that linearized inversion yields excellent dispersion results for well-constrained *S* wave velocity profiles. To determine the *S* wave velocity structure of the firn and underlying ice from the surface wave velocities, we applied the linearized inversion code suggested by *Herrmann* [2013]. Our strategy of inversion is guided, seeking iteratively for solutions that are linearly close to an *S* wave reference model [*Parker*, 1994]. In our case, the reference or initial model is the output of the traveltime inversion described in the previous section. This procedure allows us to identify a reliable solution that fits the surface wave data and facilitates the computation of the associated errors [*Gabriels et al.*, 1987]. To this end, an *S* wave model is set up and used to calculate the surface wave velocities, which are compared with the picked velocities. Hence, the *S* wave model that best fits the picked data is derived. This result is feasible because surface wave velocities depend mainly on the *SV* and *SH* wave velocities and are relatively insensitive to realistic variations in density, *P* wave velocity and quality factors with depth [*Nolet*, 1981; *Aki and Richards*, 2002].

Following *Gabriels et al.* [1987], the considered linear equations are overdetermined, and the solution is defined as the model that minimizes

$$\left\| C^{-1/2} A\beta - C^{-1/2} d \right\|, \tag{3}$$

where C is the covariance matrix of the data, β is the vector of shear wave perturbations in each layer, d is the vector of differences between calculated and measured surface wave velocities and A is a matrix of partial derivatives given by

$$A_{ij} = \frac{\partial c_j}{\partial \beta_j}, \tag{4}$$

where c_j are the surface wave velocities. As shown by *Nolet* [1981], the uncertainty in the *S* wave velocity $\Delta\beta_i$ can be estimated for uncorrelated data with

$$(\Delta\beta_i)^2 = \sum_j A_{ij}^{-1} A_{ji}^{-1} \sigma_j^2, \tag{5}$$

where A^{-1} is the generalized inverse of A and σ_j is the error in c_j, which is related to the picking of the dispersion curves. Uncertainties related to the inverted *S* wave velocities are determined by considering several different parameterizations for the inversion procedure, that is, the number of layers, the smoothness of the perturbation function and the *P* to *S* wave velocity ratio. In general, there is a trade-off between resolution (the number of layers in a certain depth range of the model) and variance. The robustness and stability of the inversion algorithm is guaranteed using a procedure similar to that described by *Cercato* [2009], which checks the dispersion curve sensitivity with respect to the applied perturbations to limit the number of inversions. Moreover, the application of smoothing constraints prevents large variations between layer velocities.

4.3. VTI Model Building

The energy (group) velocities can be observed and measured in recorded wavefields along rays [*Carcione et al.*, 2010]. We use the *P* and *S* wave velocity profiles of the firn, obtained as described in section 4.1, to estimate the energy velocity field of the underlying ice according to an optimized ray tracing algorithm based on the shooting method [*Červený*, 2001]. The algorithm consists in an iterative procedure that performs a ray tracing of the waves reflected at the ice bottom and minimizes the difference between the computed and picked traveltimes, as well as the difference between the actual offset and computed offset at which each traced ray emerges at surface. For a given ray, the algorithm updates the ice energy velocity and propagation angle at each iteration. This enables the estimation of the average *P*, *SV*, and *SH* wave velocities over a wide range of energy propagation angles. Then, we search for a VTI model that is compatible with the observed experimental velocities. This model can be obtained by fitting the energy velocities computed along the longitudinal and transverse profiles. In the case of VTI media, for which the symmetry axis is vertical, the components of the seismic wavefield are defined as follows: quasi-compressional (*qP*) waves, vertically polarized

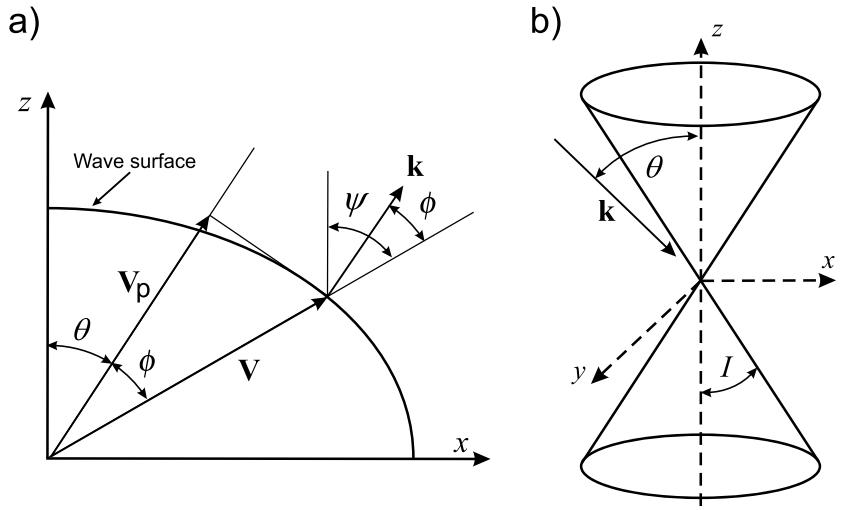

Figure 5. (a) Relation between the energy velocity vector **v**, phase velocity vector $\mathbf{v}_p$, and wave number vector **k** in terms of the phase angle θ and energy angle ψ, where $\phi = \psi - \theta$ (modified from *Carcione* [2015]). (b) Geometry of conical ice crystal *c* axes distribution (adapted from *Blankenship and Bentley* [1987]).

quasi-shear *qSV* waves, and *SH* waves. Appendix A describes in detail the propagation properties of *qP*, *qSV*, and *SH* waves.

Let us consider the (x, z) plane of a VTI medium. The elastic constants c_{IJ}, $I, J = 1, \ldots, 6$, can be obtained from five energy velocity values

$$
\begin{aligned}
c_{11} &= \rho v_{qP}^2(90^\circ) \\
c_{33} &= \rho v_{qP}^2(0^\circ) \\
c_{44} &= \rho v_{SH}^2(0^\circ) = c_{55} = \rho v_{qSV}^2(0^\circ) = \rho v_{qSV}^2(90^\circ) \\
c_{66} &= \rho v_{SH}^2(90^\circ) \\
c_{13} &= -c_{55} + \frac{1}{l_1 l_3}\sqrt{\left(c_{11}l_1^2 + c_{55}l_3^2 - \rho v_{pqP}^2\right)\left(c_{55}l_1^2 + c_{33}l_3^2 - \rho v_{pqP}^2\right)},
\end{aligned}
\tag{6}
$$

[*Carcione*, 2015], where v_{qP}, v_{qSV}, and v_{SH} are the measured energy velocities at a given energy angle ψ, and ρ is the density. Moreover, $l_1 = \sin\theta$ and $l_3 = \cos\theta$ are the direction cosines, where θ is the phase angle between the wave number vector (orthogonal to the wave surface) and the symmetry axis. The relation between the phase and energy velocities and between the corresponding angles θ and ψ is shown in Figure 5a and explained in Appendix A.

The *qP* wave phase velocity v_{pqP} in equation (6) is obtained from the measured energy velocity v_{qP} at $\psi = 45^\circ$ using equation (A8) or

$$
v_{pqP} = \frac{v_{qP}(45^\circ)}{\sqrt{2}}(l_1 + l_3), \tag{7}
$$

[*Carcione*, 2015], where the corresponding phase angle θ can be determined from ψ using equation (A3).

To find the best VTI model fitting the energy velocities computed using the ray tracing minimizing method, we vary the energy velocity values in equation (6) within appropriate intervals. Equations (A2) and (A6) allow us to find the best fit at all energy angles ψ using standard multiple regression techniques. Once the elastic constants corresponding to the best fit are determined, the phase velocities as a function of the phase angle θ are given by equation (A1).

Table 1. Single Crystal Ice Coefficients (a_i, b_i, and c_i) and Results of the Analysis, Where T, I, and q Are the Average Temperature, Cone Angle, and Anisotropic Ice Fraction of the Whole Ice Column[a]

Source	a_1	b_1	c_1	a_2	b_2	a_3	b_3	T	I	q(%)
Jona and Scherrer [1952]	257.19	5.02	5.28	498	36.8	528.13	7.93	−14.8	72.4	97
Green and McKinnon [1956]	262.99	5.35	4.69	493.66	35.57	515.49	14.54	−15.4	71.0	98
Bass et al. [1957]	265.55	7.59	4.55	495.96	49.18	529.19	17.74	−16.6	75.6	92
Brockamp and Querfurth [1965]	260.67	7.07	5.84	497.58	49.2	531.2	17.54	−15.7	74.7	97
Dantl [1968]	262.94	5.25	6.01	520.43	41.17	546.67	16.23	−14.6	74.3	97
Bennett [1968]	256.28	5.92	5.08	501.97	45.37	531.40	15.94	−15.6	73.1	94
Gammon et al. [1983]	257.75	6.14	4.91	503.90	45.88	534.07	17.41	−15.8	74.0	95

[a]The coefficients a_i, b_i, and c_i have been computed using the elasticity tensors provided by different authors, as described in Appendix C.

Finally, to quantify the anisotropy of the ice, we use Thomsen's coefficients [*Thomsen*, 1986]:

$$\epsilon = \frac{c_{11} - c_{33}}{2c_{33}},$$
$$\gamma = \frac{c_{66} - c_{55}}{2c_{55}}, \tag{8}$$
$$\delta = \frac{(c_{13} + c_{55})^2 - (c_{33} - c_{55})^2}{2c_{33}(c_{33} - c_{55})}.$$

4.4. COF Model Building

Estimates of both the mean temperature and fabric properties of ice sheets and ice streams can be obtained from active-source seismic measurements [e.g., *Blankenship and Bentley*, 1987]. The body wave slowness surfaces, simply defined as the inverse of the phase velocities, can be related to the fundamental elastic properties of the ice. Consider an ice mass at temperature T composed of polycrystalline ice in which the c axes are spaced evenly throughout a cone of apex angle I. The apex angle is defined as the angle between the vertical symmetry axis and the generatrix (Figure 5b). If the ice mass is composed of both homogeneous isotropic ice and anisotropic VTI ice, the average slowness over a straight line path, $S(\theta)$, can be expressed as

$$S(\theta, T, q, I) = S_{\text{iso}}(T) + q\left[S(\theta, T_0, I) - S_{\text{iso}}(T_0)\right], \tag{9}$$

[*Bennett*, 1968; *Blankenship and Bentley*, 1987], where q is the fraction of ice that is anisotropic. The average slowness surface $S(\theta, T_0, I)$ of qP, qSV, and SH waves at a reference temperature T_0 can be approximated using equation (C1), which depends on the empirical coefficients for ice crystals listed in Table 1. These coefficients have been computed, using the elastic tensors provided by different authors, as described in Appendix C. The slowness $S_{\text{iso}}(T_0)$ in isotropic ice at the reference temperature T_0 is calculated from equation (C1) with $I = 90°$. Moreover, the slowness $S_{\text{iso}}(T)$ in isotropic ice at temperature T can be computed using equation (C3).

Before building the COF model, we first compute, as described in the previous section, the energy velocities along the longitudinal and transverse profiles and determine whether the anisotropic velocity model of the ice mass is effectively VTI. Then, equation (9), together with equations (A8) and (A9), allow T, q, and I to be uniquely determined using standard multiple regression techniques.

5. Results

5.1. Diving-Wave Traveltime Inversion of *P* and *S* Waves

To derive the vertical velocity gradient of the firn, we need to pick the diving-wave first-break traveltimes of the shallow-refraction records shown in Figure 2, acquired using the hammer source. The average dominant frequency f_d of the diving-wave first arrivals (defined as the average frequency centroid of the seismic wavelets) is approximately 160 Hz for the P waves and 80 Hz for the S waves, respectively. Assigning an error of $T_d/4$ (where $T_d = 1/f_d$ is the dominant period) to the picked traveltimes and accounting for additional errors due to source and receiver positioning, the corresponding average errors are approximately 2.5 ms and 3.5 ms, respectively. Then, we interpolate the picked points using a smoothing function and find that the difference between the SH wave and SV wave traveltime curves is always within the experimental errors. This finding implies that the SH and SV wave velocity functions coincide within the experimental errors. Thus, the shear

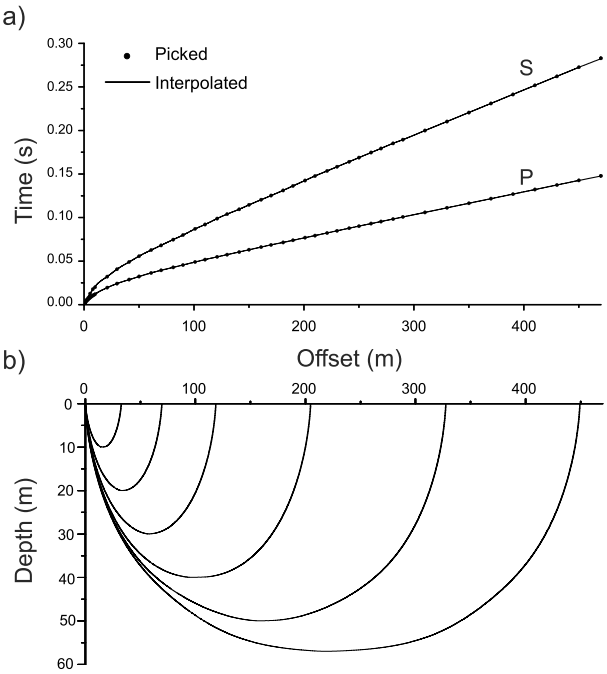

Figure 6. (a) Interpolated diving-wave first-break traveltimes picked on the shallow-refraction shot records and (b) *P* wave diving waves corresponding to certain picked first breaks.

wave splitting is negligible, and the firn can be considered isotropic. To compute the *S* wave velocity function versus depth, we take the average of the two traveltime curves, which is displayed in Figure 6a.

Figure 6b shows the diving rays corresponding to some picked points selected from those represented in Figure 6a, and Figure 7a shows the result of the traveltime inversion obtained both for the *P* and *S* waves using the Herglotz-Wiechert method described in section 4.1. The maximum *P* and *S* wave velocities, verified using the diving-wave first arrivals at larger offsets on the seismograms acquired from the explosive source, are 3864 ± 15 m/s and 1947 ± 20 m/s, respectively, at a depth of 60 ± 5 m. The errors increase to approximately ± 40 m/s at short offsets, because of the very steep gradient close to the surface. Considering that the modeled average temperature at 60 m depth is approximately −24°C (M. Bougamont, personal communication, 2014), these values agree, within the experimental errors, with the theoretical *P* and *S* wave velocities predicted by equation (C3), which are 3850 m/s and 1944 m/s, respectively. Figure 7b presents the density function versus depth calculated using the empirical relationship of *Kohnen* [1972]:

$$\rho(z) = 0.917\left[1 + \left(\frac{V_{P,\mathrm{ice}} - V_P(z)}{2.25}\right)^{1.22}\right]^{-1}, \tag{10}$$

where $V_{P,\mathrm{ice}}$ is the ice *P* wave velocity, which we assume is equal to the maximum computed *P* wave velocity.

These curves are obtained using the shallow-refraction data acquired in a single location (Figure 1b). However, we perform a ray tracing of the diving waves (Figure 6b) along all of the acquired profiles and verify the general consistency of these curves within the experimental errors. A few mismatches, due to the presence of crevasses, are compensated for using static corrections. The consistency of the results obtained from the diving-wave ray tracing along the longitudinal and transverse profiles suggests that the ice at the base of the firn layer is VTI.

5.2. Surface Wave Dispersion Analysis

To define the anisotropic characteristics of the ice below the firn, we inverted the dispersion curves of the surface wave fundamental and higher modes using the method described in section 4.2. The seismic data show a well-developed surface wave fan (Figure 3) with a coherent dispersion typical of the propagation through a 1-D simple layered medium. Figure 8 shows the Rayleigh and Love wave dispersion spectra obtained from a slant stack of the recorded wavefield. This 2-D transform is applied to the vertical, horizontal longitudinal, and transverse components in the frequency range from 1 to 50 Hz to determine the fundamental and higher modes for the orthogonal seismic profiles.

The interpretation of the modal identity is based on a conventional method for inverting surface waves [*Gabriels et al.*, 1987]. Rayleigh and Love fundamental and higher modes are picked in the surface wave velocity-frequency domain for the longitudinal (Figures 8a and 8c) and transverse (Figures 8b and 8d) profiles. The scattered black dots on the phase velocity spectra of Figure 8 represent all possible dispersion curves obtained by applying the automatic picking routine suggested by *McMechan and Yedlin* [1981].

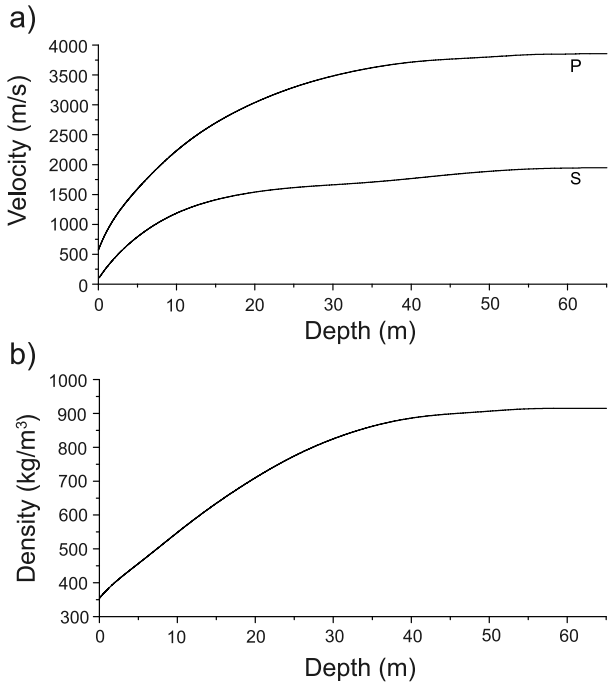

Figure 7. (a) *P* and *S* wave velocity profiles versus depth obtained using the Hergloz-Wiechert traveltime inversion method and (b) density profile obtained from the *P* wave velocity profile, using equation (10).

The fundamental modes are typically characterized by the largest spectral amplitudes. The Rayleigh wave fundamental mode (Figures 8a and 8b) has larger spectral amplitudes than the Love wave fundamental mode (Figures 8c and 8d). The latter can be easily defined at frequencies below 10 Hz, whereas the modal pattern is difficult to interpret at higher frequencies. These interpretation problems are often observed at higher frequencies because material property contrasts in the shallow structures produce wavefields with dominant higher modes and osculation points. The results from the traveltime inversion of diving waves (see section 5.1) help to establish a reference *S* wave velocity model, for which the surface wave dispersion curves are calculated and compared with the observed modal pattern. This process allows us to check the picking of the different modes to avoid misidentification. The interpreted modes used in the following inversion procedure are labeled and indicated by the white segments in Figure 8.

The velocity error Δc is obtained directly from the values of the coherence function in the dispersion spectra shown in Figure 8. It is proportional to the square of the surface wave velocity c, according to the relation $\Delta c = \sigma c^2$, where σ is the standard error of the ray parameter normal distribution estimated from the coherence function. More details regarding the error estimation can be found in *Herrmann* [2013]. The interpreted modes, in terms of surface wave velocity-frequency values and associated standard errors, are shown in Figure 9a.

Because accurate surface wave velocity measurements have been obtained in the frequency range from $\approx$ 2 Hz to 25 Hz, reliable *S* wave velocity models can be theoretically determined down to a depth of approximately 300 m. This limit is useful for both constraining the *S* wave velocities within the firn and defining the velocities within the deeper ice. The phase velocity curves of the Rayleigh and Love fundamental modes are well separated with no overlapping error bars and coincide for each of the different orthogonal profiles, as shown in Figure 9a. We first perform a Rayleigh wave dispersion data inversion using the linearized method described in section 4.2. The initial models are derived from the Hergoltz-Wiechert traveltime inversion up to 65 m depth and from the available literature on the seismic properties of polar firn [*Bennett*, 1972; *Kohnen and Bentley*, 1973; *King and Jarvis*, 2007]. The average ice stream thickness is held constant in the inversion at approximately 780 m, as estimated from the ice-penetrating radar data acquired during the same expedition [*Christianson et al.*, 2012]. The number and increasing thickness ratio of the layers are selected by considering the rules of thumb described in *Xia et al.* [1999]. To evaluate the stability of the results and the induced error, several inversion runs of 10–20 iterations each were performed using different starting models along with different smoothing and damping values. The constrained linear inversion provides a number of possible models, which display sharp velocity gradients and theoretical dispersion curves consistent with the observations. All of the preliminary *S* wave velocity models obtained by inverting the Rayleigh wave fundamental and first higher modes are used to calculate the synthetic Love wave fundamental mode. It is not possible to find a synthetic Love wave fundamental mode compatible with the observed Love wave dispersion data by overlapping the obtained curves. An example of this misfit is given in Figure 9a, where the solid line represents the Love wave velocities obtained from a *S* wave model that fits the observed Rayleigh wave velocities. The observed and synthetic Love wave phase velocities clearly do not match. Thus, a single isotropic model is not able to jointly fit both Rayleigh and Love wave velocities. This finding is in agreement with *Crampin* [2011],

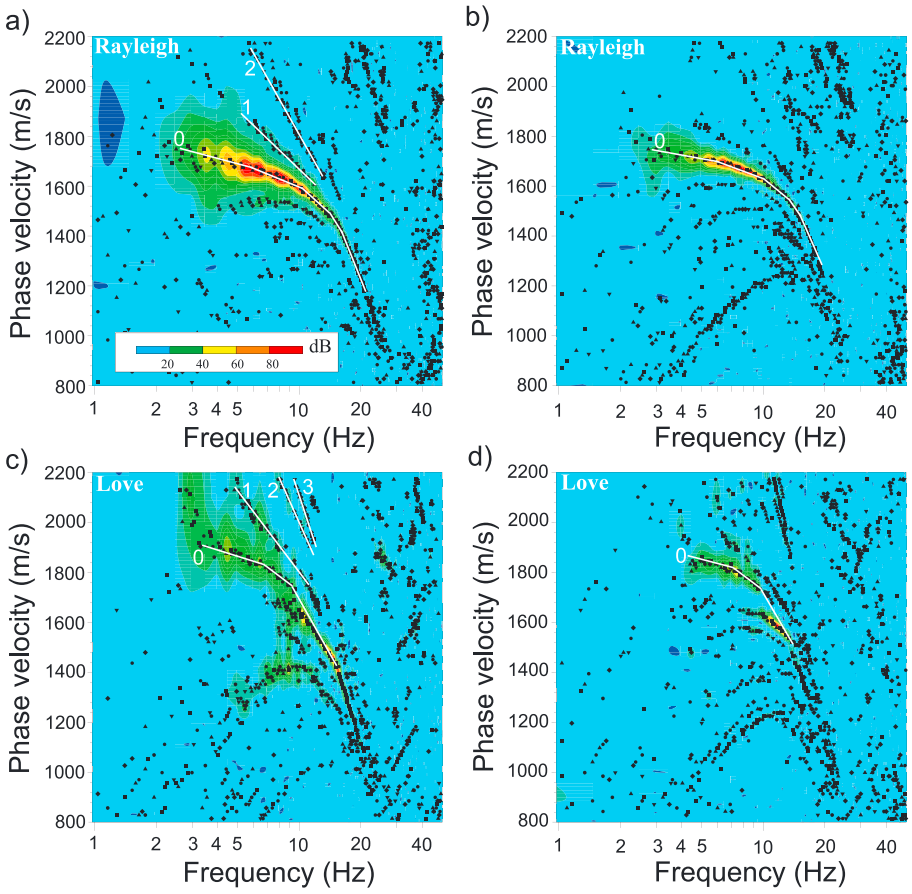

Figure 8. Surface wave velocity spectra for the (a, c) longitudinal and (b, d) transverse profiles, where only the 2-D transform of the vertical (Figures 8a and 8b) and horizontal transverse (Figures 8c and 8d) components are shown. The 2-D transform of the horizontal longitudinal component is very similar to Figures 8a and 8b. The black symbols indicate the picking of Rayleigh (Figures 8a and 8b) and Love (Figures 8c and 8d) fundamental and higher modes. White numbers and segments indicate the interpreted modes used in the inversion procedure. The colors indicate the stack values.

who reported that Rayleigh and Love wave velocities are mutually incompatible with a single isotropic model when the medium is effectively anisotropic. Thus, we proceed to invert the observed Love wave dispersion curves by using the same input parameterization used for the Rayleigh waves. The first 65 m are constrained to vary smoothly in the inversion procedure because large differences in the surface wave fundamental modes are mainly observed below 10 Hz. During the inversion process, the largest *S* wave velocity perturbations are allowed for layers within the depth range from 65 to 300 m. Figure 9b shows the final *SV* and *SH* wave velocity profiles versus depth obtained by separately inverting the Rayleigh and Love fundamental and first higher modes, respectively. The results are shown down to a maximum depth of 200 m because below this depth, the associated errors are excessive and the results are not reliable. In the firn depth interval (0–65 m), the *SV* and *SH* wave velocity curves from the surface wave dispersion analysis match quite well with the velocities derived through the traveltime inversion of diving waves (which uses the data from the hammer shallow-refraction experiment). The uncertainty in the *S* wave profiling is related to the wavelength and to the different levels of accuracy in measuring the surface wave dispersion curves shown in Figure 8. The error bars associated with the *SV* and *SH* wave velocity curves are smaller in the shallow part of the firn than at larger depths because the wavelengths sampling the deeper parts are much larger than those sampling the firn. Moreover, the *SH* wave velocities derived from Love waves show larger uncertainties than the *SV* wave velocities obtained from Rayleigh waves because of the higher degree of scatter of the picked Love wave points in the velocity spectra shown in Figure 8, particularly for frequencies below 10 Hz.

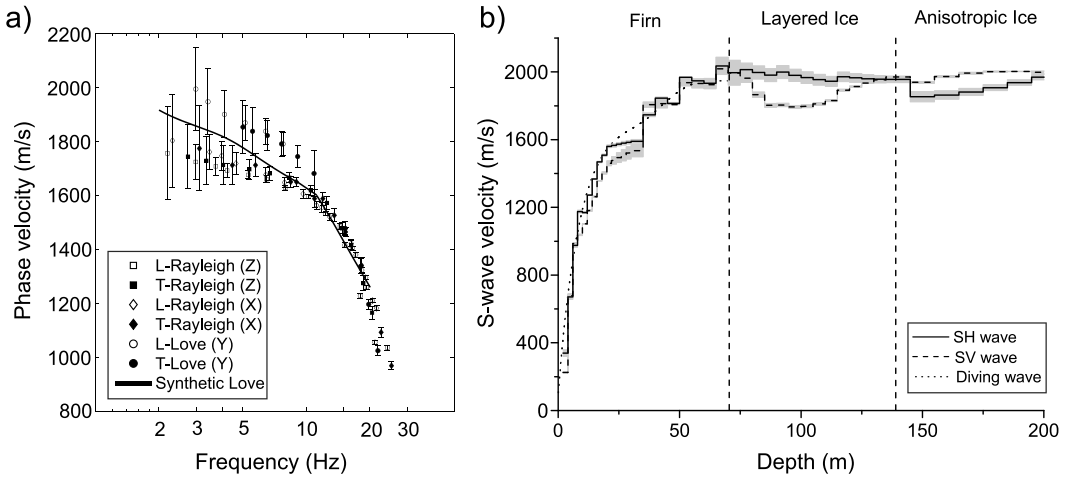

Figure 9. (a) Rayleigh and Love wave velocity points and error bars picked from Figure 8 on the orthogonal seismic profiles. (b) *SV* and *SH* wave velocity profiles obtained by separately inverting Rayleigh and Love wave fundamental and first higher modes, respectively. The data plotted in Figure 9a correspond to the vertical (*Z*), horizontal longitudinal (*X*), and transverse (*Y*) components of the fundamental mode, and belong to the longitudinal (L) and transverse (T) profiles. Moreover, the solid line indicates the synthetic Love wave fundamental mode obtained from the Rayleigh wave, which does not match with the observed Love wave velocities. The dotted line in Figure 9b represents the firn *S* wave velocity profile obtained from the Hergoltz-Wiechert traveltime inversion (see section 5.1), whereas the grey bands represent the uncertainty. The firn layer and the ice at the base of the firn are nearly isotropic, whereas the percent *S* wave anisotropy increases to a mean value of approximately 3.4% between 140 m and 200 m depth. The analysis of surface waves also indicates the likely presence of layered ice beneath the firn, down to a depth of approximately 140 m (see sections 5.2, 5.3, and 6 for details).

5.3. VTI and COF Models of the WIS

The results obtained from the traveltime and surface wave dispersion inversions (Figures 7a and 9b) show that, within our level of accuracy, no anisotropy is observed in the firn, whereas it is evident below approximately 65 m depth, where the *SV* and *SH* wave velocities become substantially different. Moreover, the consistency of the results obtained from the surface wave dispersion inversion along the longitudinal and transverse profiles show that, within the experimental errors, the ice below the firn is VTI. The average velocities of the horizontally traveling *qSV* and *SH* waves between 65 m and 140 m depth are $v_{qSV}(90°) = 1880 \pm 10$ m/s and $v_{SH}(90°) = 1974 \pm 36$ m/s, respectively. Similarly, the average *qSV* and *SH* wave velocities between 140 m and 200 m are $v_{qSV}(90°) = 1982 \pm 10$ m/s and $v_{SH}(90°) = 1916 \pm 20$ m/s, respectively. The difference between $v_{qSV}(90°)$ and $v_{SH}(90°)$, which is due to shear wave splitting, is often reported as a percent anisotropy k_S, calculated as [e.g., *Savage*, 1999]

$$|k_S| = 200 \frac{\left|v_{SH}(90°) - v_{qSV}(90°)\right|}{v_{SH}(90°) + v_{qSV}(90°)}. \tag{11}$$

The value of $|k_S|$ is approximately 3.8% between 65 m and 140 m and 3.4% between 140 m and 200 m. Similar values of percent anisotropy have been observed in many geological formations. *Crampin* [1994] and *Savage* [1999] reviewed the worldwide evidence for crustal anisotropy and concluded that the percentage anisotropy in the upper 10–15 km of the crust is typically 1.5–4%. It is remarkable to observe similar values for the ice in this study.

The *S* wave anisotropy derived from the surface wave analysis may be used to infer the crystal fabric properties between 65 m and 200 m depth. Considering that the average modeled temperature is approximately −23°C in this depth range (M. Bougamont, personal communication, 2014), we plot in Figure 10 the horizontal *S* wave velocities versus cone angle using the COF model described in section 4.4, according to the empirical coefficients for ice crystals provided by several authors (Table 1). For a cone angle of approximately 63.5° and $q \approx 100\%$, the *S* wave velocities derived from the surface wave analysis between 140 m and 200 m depth correspond well with the theoretical wave velocities obtained by using the elastic coefficients of *Bass et al.* [1957], as shown in Figure 10. In contrast, these COF models are unable to explain the *S* wave velocities

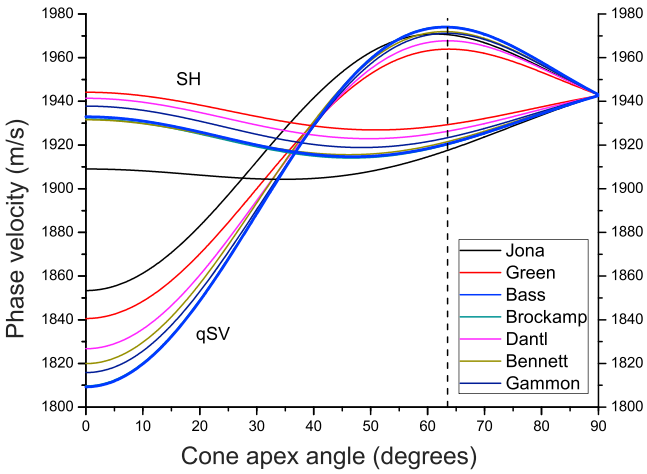

Figure 10. COF models for the horizontal *qSV* and *SH* wave velocities corresponding to a temperature of −23°C. The different curves correspond to the empirical coefficients for ice crystals provided by several authors (Table 1). In correspondence to a cone angle of approximately 63.5° (vertical dashed line), the *S* wave velocities derived from the surface wave analysis between 140 m and 200 m depth correspond well with the theoretical velocities obtained by using the elastic coefficients provided by *Bass et al.* [1957] (blue thick line).

obtained between 65 m and 140 m depth because they indicate cone angles that are too tight (approximately 22°), where the values in this depth range are typically higher than 50° [*Pettit et al.*, 2007].

Next, we use the *P* and *S* wave velocity profiles of the firn shown in Figure 7a and the forward ray tracing minimizing method described in section 4.3 to compute the average *P*, *SV*, and *SH* wave velocities of the entire ice column below the firn for a wide range of energy propagation angles. Detailed knowledge of the bed morphology, as estimated to a precision of ±8 m from the ice-penetrating radar data acquired during the same expedition [*Christianson et al.*, 2012], and the fact that surface and bed slopes are always less than 1°, allow for an accurate computation of the energy velocities. We obtain the anisotropic velocity structure of the ice stream using the following procedure. First, we pick the traveltimes of *P*, *SV*, and *SH* and converted *P-SV* waves reflected from the bed along the longitudinal and the three transverse profiles. The first breaks of the reflected *P* waves are picked on both the data recorded using standard geophones at short and medium offsets and the vertical component recorded by the 3C stations at long offsets (Figure 4a). Similarly, the first breaks of the reflected *SV* and *SH* waves are picked, respectively, on the horizontal longitudinal and transverse components recorded by the 3C stations (Figures 4b and 4c). Unfortunately it was not possible to pick the reflected events of the *SV* waves along the longitudinal profile; however on the horizontal longitudinal component we picked the first breaks of the converted *P-SV* waves at the ice bottom interface and reflected to the surface. Since the signal/noise ratio of the *P* waves is very high, it is possible to pick the first breaks of the reflected seismic events directly. However, because of the lower signal/noise ratio of the *S* waves, we pick the maximum of the trace envelope of the reflected seismic wavelets, which is a good approximation of the wavelet centroid. An example of picking is given in Figures 11a and 11b, where some reflected *SH* waves are shown. We discard the worst traces (approximately 20% of the traces in the selected offset ranges), and then fit the picked traveltimes using a smoothing function to reduce the dispersion of the picked points due to noise and other factors (e.g., the presence of crevasses in the shallow firn and source and receiver positioning). The error in the picked traveltimes is evaluated by considering both the frequency content and the signal/noise ratio. Figure 11c shows a typical spectrum of the reflected *P* and *S* wavelets. The average dominant frequency f_d is approximately 200 Hz for the *P* waves recorded by the standard geophones and 115 Hz and 60 Hz for the *P* and *S* waves recorded by the 3C stations, respectively. Seismic wave attenuation is typically very low in polar ice, as confirmed, for example, by *Bentley and Kohnen* [1976], who measured a *P* wave quality factor ranging from 500 to 1700 at Byrd Station (West Antarctica). These measurements were performed at a temperature (−28°C) and average frequency (136 Hz) very similar to those of our experiment. Thus, the frequency content remains nearly constant along the reflected events. Assigning an error of $T_d/4$ to the picked traveltimes, the corresponding errors are approximately 1.3 ms, 2.2 ms, and 4.2 ms, respectively. The error due to noise is evaluated by computing the residuals resulting from the fit of the picked points (Figure 11d). The standard deviations are 1 ms for the *P* waves recorded by the standard geophones, and 3 ms and 8 ms for the *P* and *S* waves recorded by the 3C stations, respectively. Considering that the half width of a Ricker wavelet with a dominant frequency f_d is approximately $1.5T_d$ [*Carcione*, 2015], we subtract $1.5T_d$ from the picked traveltimes to obtain the first breaks. Figures 11a and 11b show the good fit of the first breaks obtained using this value. The forward ray tracing minimizing method is then applied along the orthogonal profiles to determine the *P* wave energy velocities between 0° and approximately 75°, and the *SV* and *SH* wave energy velocities between approximately 25° and 65°. We use the already derived *P* wave velocities

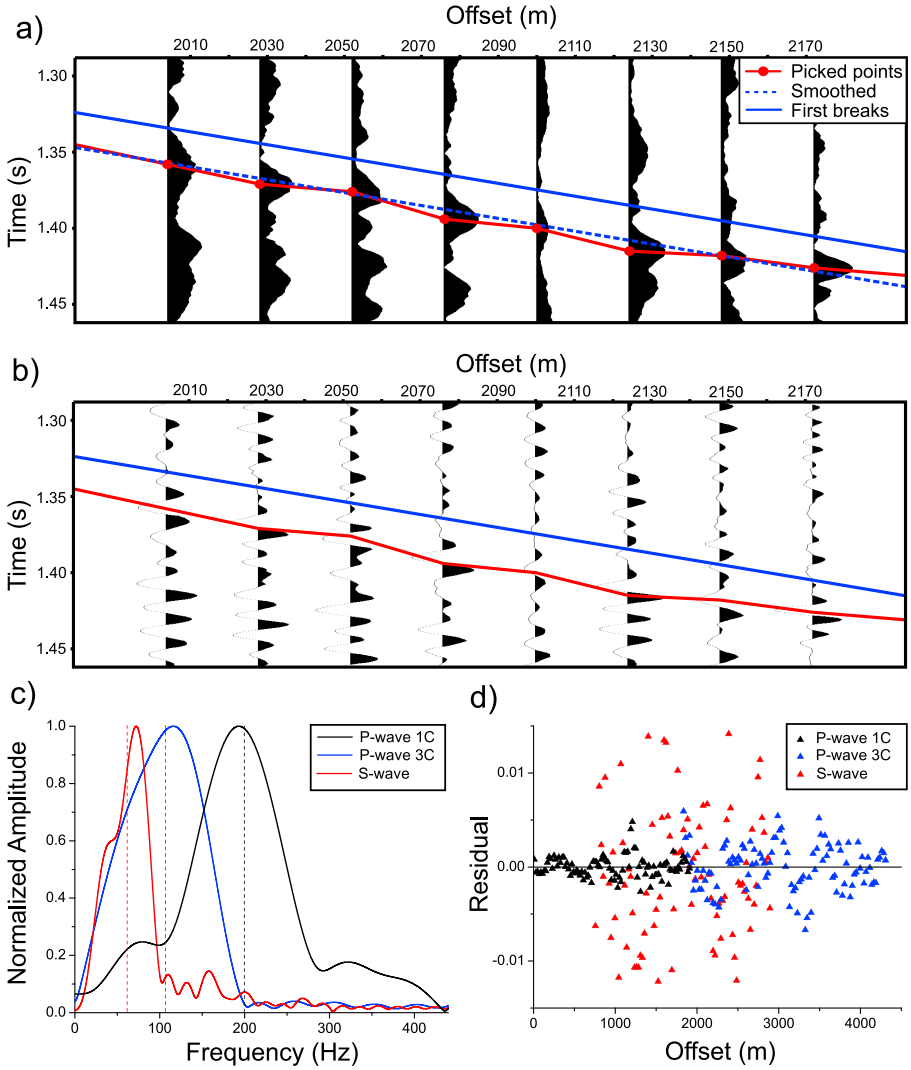

Figure 11. Example of picking of the *SH* wave reflected traveltimes (a) on the trace envelopes and (b) on the corresponding original traces of the ensemble shown in Figure 4c. The maximum of the trace envelope is first picked (red dots and line), then the picks are fitted using a smoothing function (blue dashed line) and $1.5T_d$ is subtracted to obtain the first breaks (blue solid line). (c) Typical spectra of the reflected wavelets and (d) residuals from the fit of the picked *P* and *S* reflected arrivals.

to compute the ray tracing for the P-SV reflected events. Figure 12 shows an example of the ray tracing of *P* waves and converted *P-SV* waves reflected from the bed, where a blowup shows how the rays bend as they approach the surface because of the strong velocity gradient in the firn (Figure 7a). The resulting average velocity errors are approximately 15 m/s for the *P* waves and approximately 20 m/s for the *S* waves. Then, by applying a standard multiple regression technique, we fit the computed energy velocities together using the VTI and COF models described in sections 4.3 and 4.4.

Figure 13 displays the experimental energy velocities (triangles) along the longitudinal (a and c) and transverse (b and d) profiles derived by the ray tracing minimizing method using the picked traveltimes of the reflected waves. Additionally, the energy velocities for the corresponding best fits using the VTI and COF models are shown. The differences between the VTI best fit and the experimental velocities are below the estimated errors. Hence, the experimental velocities can be explained with a VTI model. Considering a density of $\rho_{ice} = 0.917$ kg/m^3 for the ice, the five elastic constants c_{IJ} in equation (6), corresponding to the best fit, are as follows: $c_{11} = 13.43 \pm 0.21$ GPa, $c_{33} = 13.36 \pm 0.21$ GPa, $c_{13} = 6.64 \pm 0.14$ GPa, $c_{55} = 3.50 \pm 0.14$ GPa, and $c_{66} = 3.38 \pm 0.14$ GPa. These elastic coefficients yeld the following Thomsen parameters expressed by equation (8): $\epsilon = 0.003$, $\gamma = -0.017$,and $\delta = 0.021$, which correspond to a weak anisotropy [*Thomsen*, 1986].

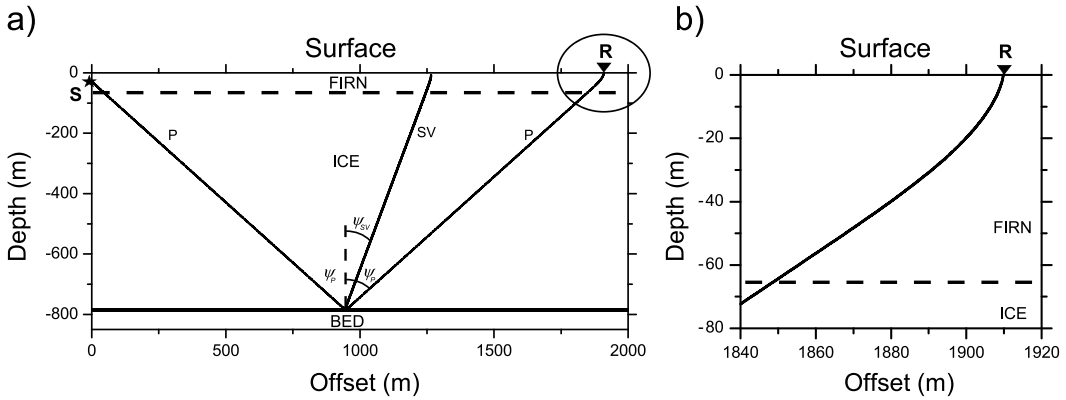

Figure 12. (a) Ray tracing of the *P* wave and the converted *P-SV* wave reflected from the bed, traveling at approximately $\psi_P = 50°$ and $\psi_{SV} = 23°$ energy propagation angles, respectively. (b) Blowup of the *P* wave ray emerging at the surface, in the zone evidenced by the circle in Figure 12a, showing the bending caused by the velocity gradient in the firn. The source (S) and receiver (R) are indicated. Surface and bed slopes are always less than 1°.

Figure 13 also shows the fits obtained using the COF model, according to the coefficients provided by several authors listed in Table 1. The average ice sheet temperature *T*, cone-apex angle *I*, and anisotropy ice fraction *q* corresponding to each fit are also reported in Table 1.

Because the differences between the experimental velocities and computed fits are below the estimated errors, the seven plotted models are all compatible with the observed experimental velocities, which also

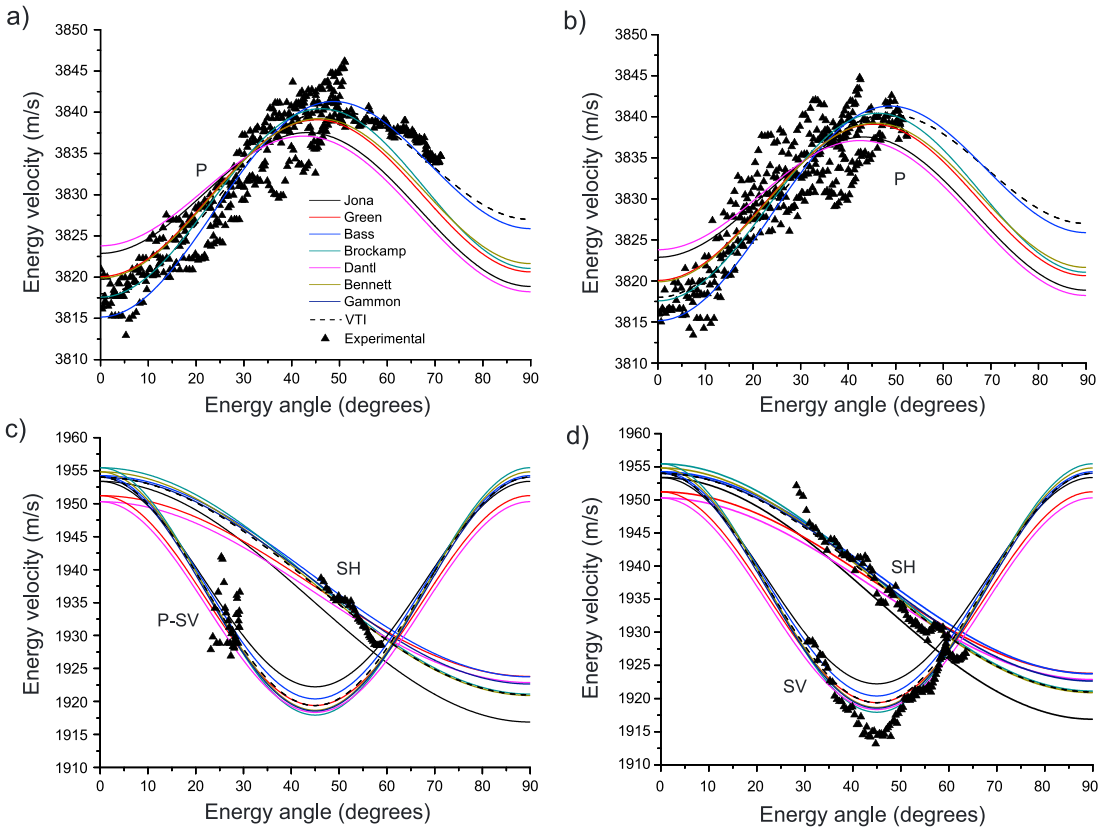

Figure 13. Fit of the *P*, *SV*, and *SH* wave energy velocities (triangles) computed for the (a, c) longitudinal and (b, d) transverse profiles using the COF (solid lines) and VTI (dashed lines) models. The *SV* wave velocity values at small angles (between 25° and 30°) represented in Figure 13c correspond to the reflected events of the converted *P-SV* waves. The fits obtained using the COF models define the mean temperature and mean fabric properties of the entire ice column below the firn. The different curves correspond to the empirical coefficients for ice crystals provided by several authors (Table 1).

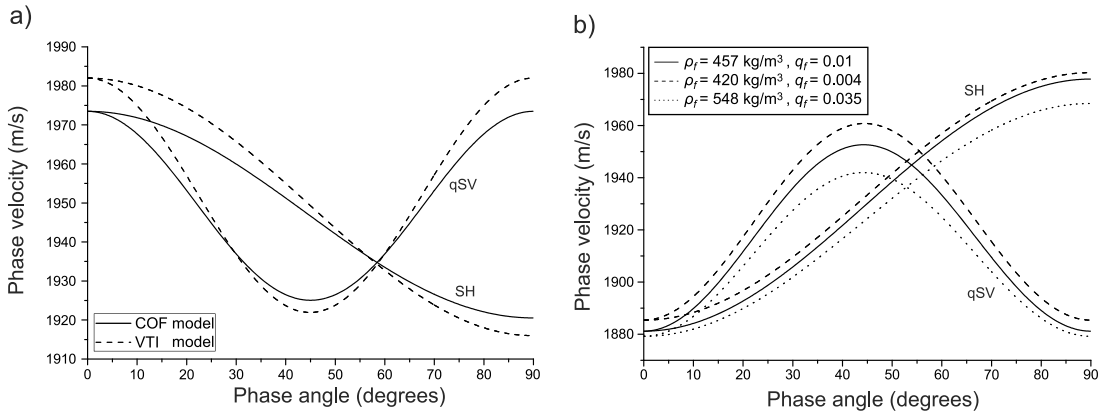

Figure 14. (a) Fit of the *S* wave phase velocities obtained from the COF model, using the VTI model. (b) *S* wave phase velocities versus phase angle obtained by using different combinations of firn density ρ_f and relative thickness q_f. The COF models use the ice crystal coefficients reported in *Bass et al.* [1957] and correspond to a temperature of −23°C and a cone angle of 63.5°. To compute the fit, we assume that the horizontal *S* wave velocities are those derived from the surface wave analysis: (i.e., $v_{qSV}(90°) = 1982 \pm 10$ m/s and $v_{SH}(90°) = 1916 \pm 20$ m/s).

reflects the fact that the temperature and fabric property values reported in Table 1 are similar to each other. Thus, we compute the most representative temperature and fabric properties by averaging the values corresponding to the seven fits, obtaining the following: $T = -15 \pm 5$°C, $I = 73 \pm 10$°, and anisotropic ice fraction $q = 95\%$. The true temperature profile for the WIS region is unknown, but a numerical evaluation can be made according to a three-dimensional high-order ice sheet model applied to the Siple Coast region [*Christoffersen et al.*, 2014]. This simulation yields a steady state modeled average ice sheet temperature (below the firn) of approximately −14°C in the region of the SLW (M. Bougamont, personal communication, 2014), which corresponds with the results of this work within the estimated experimental errors. Finally, note that the VTI model assumes that the whole ice column is anisotropic, whereas the COF model allows for some proportion of isotropic ice through the parameter *q*. The good agreement between the two models, when applied to the same data, shows that almost the whole ice column is anisotropic ($q \geq 95\%$), and thus the VTI model assumption is further justified.

6. Discussion

Seismic azimuthal anisotropy is the most common type of anisotropy observed in ice sheets and, more generally, in nearly all geologic media [*Bush and Crampin*, 1987]. In the case of ice, anisotropy is intrinsic to the medium when induced by the preferred orientation of *c* axes [*Bennett*, 1968; *Blankenship and Bentley*, 1987], whereas it might depend on the texture of the medium when there are fractures aligned along a preferential direction [*Santos et al.*, 2012; *Carcione et al.*, 2012, 2013] or in the presence of laminated media [*Backus*, 1962; *Slack et al.*, 1993; *Carcione*, 2015]. In analogy to crust seismology, this distinction corresponds to the lattice-preferred orientation/shape-preferred orientation distinction [*Mainprice and Nicolas*, 1989]. Hence, the anisotropic character of an ice stream can be represented by either a VTI model or azimuthally anisotropic model. The VTI structure is typically observed in correspondence of ice domes and ice divides [e.g., *Blankenship and Bentley*, 1987], where the flow is transversely divergent or neutral [*Alley*, 1988], but it has also been observed on fast-flowing ice streams [e.g., *Anandakrishnan*, 1999]. Below a certain depth, in regions where englacial deformation dominates because of strong interactions with a pronounced bed topography, and in particular upstream of bedrock features, *c* axes are induced to rotate away from the vertical in the direction of flow [*Bentley*, 1971; *Horgan et al.*, 2011]. Similarly, this process occurs away from ice domes and ice divides, in the presence of bedrock or poorly lubricated basal sediments, and close to the grounding line, where longitudinal deviatoric stresses can be important [*MacAyeal*, 1989]. In these cases, azimuthal anisotropy might be observed, as well as englacial seismic reflections, which may indicate abrupt changes in the COF [*Anandakrishnan*, 1996; *Horgan et al.*, 2008, 2011; *Hofstede et al.*, 2013]. Longitudinal deviatoric stresses decrease rapidly going from the grounding line toward the interior [*Pattyn*, 2000]. Far enough from the grounding line, COF is mainly influenced by vertical compression and simple shear parallel to the bed rather than transversely compressive flow. In these conditions, in regions where basal shear stress is very low and slid-

ing is dominant, COF profiles are expected to be similar to those observed at ice divides, exhibiting properties similar to those of VTI media.

Before evaluating the COF properties from seismic anisotropy, any texture-dependent anisotropic effect that may distort the intrinsic anisotropy observed from the surface should be considered. Surface wave dispersion analysis provides an initial indication of the character of the observed anisotropy and its causal factors, such as crystal alignments or crack distributions that may be related to important ice sheet dynamics in the shallow 200–300 m. In our case, considering the experimental errors, *S* wave anisotropy is the same for the longitudinal and transverse profiles, indicating that the ice beneath the firn is VTI. The analysis of the body waves reflected from the bed confirms that the anisotropic character of the entire ice column is VTI and shows that the most likely structure is one containing 95% anisotropic ice with $I = 73 \pm 10°$. Therefore, from a rheological perspective, the ice column at the SLW location is not as anisotropic as at ice domes and ice divides even though it exhibits the same VTI structure. In fact, COF measurements from regions where the fabric is symmetrical in the vertical direction (e.g., Dome C) suggest that, because of the often observed trend of decreasing cone angle with depth, the resulting average *I* is generally lower than 30° [*Blankenship and Bentley*, 1987; *Durand et al.*, 2009]. Similar results have also been obtained by *Anandakrishnan* [1999] by analyzing the high-frequency events originating from basal microearthquakes in the neighboring ice stream C. He reported a weak azimuthal dependence on the delay time, which suggests a vertical symmetry axis for the fabric. Moreover, inverting the splitting data, *Anandakrishnan* [1999] found that the most probable *c* axes distribution is a broad vertical cone angle of approximately 60°.

The COF measured at a particular location on a fast-flowing ice stream is inherited from upstream, but strains in excess and recrystallization in the ice mass may generate a new fabric [*Alley*, 1988]. Therefore, in the case of WIS, the presence of abundant soft sediments and water at the bed does not directly imply that the fabric has been conserved during the flow. In fact, the analysis of seismic data previously acquired upstream of WIS, close to the Up-stream B (UpB) camp [*Blankenship et al.*, 1986, 1987], indicates that *c* axes cluster near a transverse vertical plane, reflecting the fact that the local strain is longitudinally extensional and vertically and transversely compressional [*Alley*, 1988], because the local ice flow is convergent [*MacAyeal*, 1989]. In this work we showed that at the SLW location the *c* axes distribution is azimuth independent and the anisotropic ice structure is VTI, reflecting the fact that downstream the fabric is mainly influenced by vertically compressive and transversely divergent or neutral flow, rather than transversely compressive flow [*MacAyeal*, 1989]. This implies that recrystallization likely dominates along the WIS, as noted also by *Alley* [1988]. These results also suggest that the VTI structure might be common for ice streams flowing over highly water-saturated sediments, in regions where basal shear stresses and deviatoric stresses are low, and the principal component of the ice stream movement is basal sliding or deformation in the basal sediments, rather than deformation in the ice.

Discrepancies between some results presented in this work are particularly found for the horizontally propagating *qSV* and *SH* waves in the shallow 200 m. In section 5.3 we found that the average *qSV* and *SH* wave velocities from the surface wave analysis, for the medium between 65 m and 140 m depth, are not in agreement with those resulting from ice crystal fabric models. This discrepancy can be explained by considering that surface waves have very large wavelengths and are thus sensitive to the presence of internal stratigraphy, often reported by georadar data [*Fujita et al.*, 1999; *Matsuoka et al.*, 2003] and also evidenced in this particular location [*Christianson et al.*, 2012]. Layering on a scale much finer than the dominant wavelength of the signal yields effective anisotropy [*Backus*, 1962; *Carcione*, 2015]. This result was also confirmed by *Picotti et al.* [2010, 2012], showing that at long wavelengths, the equivalent macroscopic model of a finely layered medium (where each horizontal layer can be isotropic or VTI) behaves as a VTI medium. In other words, the combination of the anisotropy due to the ice crystal fabric and the fine layering leads to a VTI medium [*Backus*, 1962; *Carcione*, 2015; *Picotti et al.*, 2010, 2012].

Here we attempt to use the *S* wave anisotropy derived from the surface wave analysis to explain the observed discrepancies between 65 m and 140 m depth by using the Backus averaging theory [*Backus*, 1962], which is briefly summarized in Appendix B. First, using the VTI model, we compute the average elastic constants of the anisotropic ice between 140 m and 200 m depth by fitting the COF curves obtained using the coefficients provided by *Bass et al.* [1957] and shown in Figure 10. To this aim, we assume that the horizontal *S* wave velocities are those derived from the surface wave analysis (i.e., $v_{qSV}(90°) = 1982 \pm 10$ m/s and $v_{SH}(90°) = 1916 \pm 20$ m/s). Figure 14a shows the good fit for the *qSV* and *SH* wave velocities, confirming

that the two models are equivalent, considering the experimental errors. Then, we assume the presence of thin lenses of isotropic firn embedded in the ice, such that the ice-firn sequence is periodic with a period much finer than the average dominant wavelength of the surface waves. By applying the Backus theory, it is possible to reproduce the horizontal *S* wave velocities derived from the surface wave analysis between 65 m and 140 m depth (i.e., $v_{qSV}(90°) = 1880 \pm 10$ m/s and $v_{SH}(90°) = 1974 \pm 36$ m/s). Figure 14b shows the *S* wave phase velocities versus phase angle obtained using different combinations of density ρ_f and the relative thickness q_f of the thin firn layers. The best combination that fits both $v_{qSV}(90°)$ and $v_{SH}(90°)$ is $\rho_f = 457$ kg/m^3 and $q_f = 0.01$. Note that the firn proportion is very low (only 1%) compared with the period of the stratification.

Therefore, a plausible explanation of these discrepancies might be the presence of stratified ice beneath the firn, due to the alternating hard and thin soft layers. The existence of such thin stratification has already been put forth to explain a drop of the vertical *S* wave velocity in the lower part of polar ice sheets [*Wittlinger and Farra*, 2012]. However, the mechanism underlying the existence of both soft and hard ice layers remains uncertain. In addition, body waves may be influenced by the eventual presence of this finely layered medium, though less so than surface waves because of the large wavelength difference.

7. Conclusions

The intrinsic anisotropy of polar ice likely results from crystal orientation fabric (COF) occurring within ice masses. Seismic methods can effectively be used to infer COF properties. Typically, ice dome and ice divide seismic observations show the presence of transversely isotropic ice with a vertical axis of symmetry (VTI). However, the ice structure may be different elsewhere because the balance of deviatoric stresses may play an important role in determining the axis of symmetry for fabrics. Moreover, the presence of fractures oriented along a preferential direction or finely internal layering may induce other anisotropic effects that can mask intrinsic anisotropy. Active three-component seismic surveys provide additional insight into the anisotropic properties of ice sheets.

In this work, surface wave dispersion analysis, ray tracing, and traveltime inversion of *P* and *S* waves are applied to the multicomponent seismic data acquired on the WIS (West Antarctica), in correspondence to the SLW, with the purpose of characterizing the fabric and anisotropic features of the ice mass versus depth. Our methodology uses different components of the seismic wavefield to partition the fabric characteristics into discrete depth ranges and distinguish between intrinsic anisotropy and texture-induced anisotropy.

Traveltime inversion of diving waves and surface wave dispersion analysis have been used to investigate the shallow 200 m of the ice stream. The firn layer and the ice at the base of the firn (at the pore close-off depth of approximately 65 m) are nearly isotropic because the diving-wave velocities does not depend to the azimuth and the *S* wave anisotropy is negligible, within the experimental errors. With increasing depth, the percent *S* wave anisotropy increases to a mean value of approximately 3.4% between 140 m and 200 m and is the same in the two directions parallel and orthogonal to the ice flow, which indicates the presence of a VTI medium beneath the firn. The analysis of surface waves also indicates the probable presence of stratified ice beneath the firn, down to a depth of approximately 140 m, due to the alternating hard and thin soft layers.

Ray tracing analysis of *P*, *SV*, converted *P-SV* and *SH* waves reflected from the bed show that the entire ice mass beneath the firn is VTI, with the following average Thomsen parameters $\epsilon = 0.003$, $\gamma = -0.017$, and $\delta = 0.021$, which correspond to a low degree of anisotropy. Therefore, from a rheological perspective, the ice column at the SLW location is not as anisotropic as at ice domes and ice divides, even though it shows the same VTI structure. Fitting the wave surface with a COF model, the following average fabric parameters are determined: a broad vertical cone angle $I = 73 \pm 10°$ with an anisotropic ice fraction $q = 95\%$. Moreover, the seismically estimated average temperature of the entire ice column below the firn is $T = -15 \pm 5°$C, which is in agreement with the results from ice sheet modeling applied to the Siple Coast region. We do not observe englacial reflectivity, which may otherwise indicate abrupt changes in the COF.

These findings denote that the VTI ice structure might be typical of large ice streams flowing over highly water-saturated sediments, in regions where basal shear stresses and deviatoric stresses are low, and the principal component of the ice stream motion is basal sliding or bed deformation, rather than deformation in the ice mass. In general, anisotropic analysis of ice can be important to determine whether a basal sliding regime or a glacial deformation regime dominates, providing additional insights into the interaction between ice

streams and the substrate over which they flow. Knowledge of such phenomena has direct implications for the predictive modeling of polar ice sheets.

Appendix A: Propagation Properties of *qP*, *qSV*, and *SH* Waves in VTI Media

The phase velocities of *qP*, *qSV* and *SH* waves traveling in a VTI medium are given, respectively, by

$$\begin{aligned} v_{pqP} &= (2\rho)^{-1/2}\sqrt{c_{11}l_1^2 + c_{33}l_3^2 + c_{55} + A} \\ v_{pqSV} &= (2\rho)^{-1/2}\sqrt{c_{11}l_1^2 + c_{33}l_3^2 + c_{55} - A} \\ v_{pSH} &= \rho^{-1/2}\sqrt{c_{66}l_1^2 + c_{55}l_3^2} \\ A &= \sqrt{[(c_{11} - c_{55})l_1^2 + (c_{55} - c_{33})l_3^2]^2 + 4[(c_{13} + c_{55})l_1 l_3]^2}. \end{aligned} \tag{A1}$$

[*Auld*, 1990; *Carcione*, 2015], where c_{IJ}, $I, J = 1, \ldots, 6$ are the elastic constants and ρ is the density. Moreover, $l_1 = \sin\theta$ and $l_3 = \cos\theta$ are the direction cosines, where θ is the phase angle between the wave number vector (orthogonal to the wave surface, see Figure 5a) and the symmetry axis. Because the intrinsic attenuation for seismic waves is very low in polar ice [e.g., *Bentley and Kohnen*, 1976], we neglect its contribution. In the following we denote the phase velocities v_{pqP}, v_{pqSV}, and v_{pSH} as v_p and the corresponding energy (group) velocities as v. The energy velocity vector $\mathbf{v}$ of the *qP* and *qSV* waves, whose magnitude is v, is given by

$$\frac{\mathbf{v}}{v_p} = (l_1 + l_3\cot\psi)^{-1}\hat{\mathbf{e}}_1 + (l_1\tan\psi + l_3)^{-1}\hat{\mathbf{e}}_3 \tag{A2}$$

[*Carcione*, 2015], where

$$\tan\psi = \frac{\beta X + \xi W}{\beta W + \xi Z} \tag{A3}$$

defines the angle ψ between the energy velocity vector and the z axis, and

$$\begin{aligned} \beta &= \mathrm{pv}\sqrt{A \pm B}, \\ \xi &= \pm\mathrm{pv}\sqrt{A \mp B}, \\ B &= c_{11}l_1^2 - c_{33}l_3^2 + c_{55}\cos 2\theta, \end{aligned} \tag{A4}$$

where the upper and lower signs in the first and second equations correspond to the *qP* and *qSV* waves, respectively. Moreover,

$$\begin{aligned} W &= c_{55}(\xi l_1 + \beta l_3), \\ X &= \beta c_{11}l_1 + \xi c_{13}l_3, \\ Z &= \beta c_{13}l_1 + \xi c_{33}l_3 \end{aligned} \tag{A5}$$

[*Carcione*, 2015], where "pv" denotes the principal value, which has to be chosen according to established criteria [e.g., *Sidler et al.*, 2008]. Figure 5a shows the relation between the energy velocity vector $\mathbf{v}$ and the phase velocity vector $\mathbf{v}_p$ in terms of the phase angle θ and the energy angle ψ.

The energy velocity of the *SH* wave is

$$\mathbf{v} = \frac{1}{\rho v_p}\left(c_{66}l_1\hat{\mathbf{e}}_1 + c_{55}l_3\hat{\mathbf{e}}_3\right) \tag{A6}$$

and

$$\tan\psi = \frac{c_{66}}{c_{55}}\tan\theta \tag{A7}$$

[*Carcione*, 2015]. In general, the phase velocity is related to the energy velocity by

$$v_p(\theta) = v(\psi)\cos(\phi), \tag{A8}$$

where $v = |\mathbf{v}|$. Moreover, the angle $\phi = \psi - \theta$, schematized in Figure 5a, is given by

$$\tan(\phi) = \frac{1}{v(\psi)}\frac{\mathrm{d}v(\psi)}{\mathrm{d}\psi} = \frac{1}{v_p(\theta)}\frac{\mathrm{d}v_p(\theta)}{\mathrm{d}\theta} = -\frac{1}{S(\theta)}\frac{\mathrm{d}S(\theta)}{\mathrm{d}\theta}, \tag{A9}$$

[*Brown et al.*, 1991; *Postma*, 1955], where $S(\theta) = 1/v_p(\theta)$ is the slowness surface.

Appendix B: Backus Averaging

A finely layered medium behaves as a homogeneous anisotropic medium at long wavelengths. When each layer is transversely isotropic, the equivalent medium is also transversely isotropic and can be described using the Backus averaging theory [*Backus*, 1962]. According to *Carcione* [2015] and *Picotti et al.* [2010, 2012], the equivalent elastic constants are defined by the following relationships:

$$\begin{aligned}
\bar{c}_{11} &= \langle c_{11} - c_{13}^2 c_{33}^{-1} \rangle + \langle c_{33}^{-1} \rangle^{-1} \langle c_{33}^{-1} c_{13} \rangle^2 \\
\bar{c}_{33} &= \langle c_{33}^{-1} \rangle^{-1} \\
\bar{c}_{13} &= \langle c_{33}^{-1} \rangle^{-1} \langle c_{33}^{-1} c_{13} \rangle \\
\bar{c}_{55} &= \langle c_{55}^{-1} \rangle^{-1} \\
\bar{c}_{66} &= \langle c_{66} \rangle .
\end{aligned} \tag{B1}$$

The thickness weighted average of a quantity a is defined as

$$\langle a \rangle = \sum_{l=1}^{L} q_l a_l = \frac{1}{D} \sum_{l=1}^{L} d_l a_l, \tag{B2}$$

where d_l is the thickness of material l and q_l is the relative thickness with respect to the period of the stratification D. In the case of a periodic sequence of two alternating layers, equations (B1) are similar to those of *Picotti et al.* [2012], who considered a generalization of the Backus averaging theory to the lossy case.

Appendix C: Coefficients for the Computation of the Polar Ice's COF Properties

Bennett [1968] showed that, for VTI polar ice, the average slowness surface $S(\theta, T_0, l)$ for *qP*, *qSV*, and *SH* waves at a reference temperature T_0 can be approximated by

$$\begin{aligned}
S_{qP}(\theta, T_0, l) &= \left(a_1 + \frac{b_1}{15} + \frac{c_1}{3} \right) + \frac{k_1}{15}(16b_1 - 10c_1) \\
&\quad - \frac{8}{5} b_1 k_2 - \sin^2(\theta)((4b_1 - c_1)k_1 - 8b_1 k_2) + b_1 \sin^4(\theta)(3k_1 - 7k_2), \\
S_{qSV}(\theta, T_0, l) &= a_3 - \frac{1}{15}(8b_2 - 5b_3)(1 + k_1) + \frac{4}{5} b_2 k_2 \\
&\quad + b_2 \sin^2(\theta) \cos^2(\theta)(3k_1 - 7k_2), \\
S_{SH}(\theta, T_0, l) &= a_3 - \frac{1}{15}(8b_2 - 5b_3)(1 + k_1) + \frac{4}{5} b_2 k_2 \\
&\quad + \sin^2(\theta)((b_2 - b_3)k_1 - b_2 k_2),
\end{aligned} \tag{C1}$$

where $k_1 = \cos(l) + \cos(l)^2$ and $k_2 = \cos(l)^3 + \cos(l)^4$. The units are μs/m, and the coefficients a_i, b_i, and c_i can empirically be derived as follows. The exact slowness surfaces for single crystals are found by taking the inverse of equations (A1), where the experimental values of the elasticity constants c_{IJ} for ice, according to several authors, are listed in Table 1 of *Gusmeroli et al.* [2012]. For a given density and reference temperature T_0, these slowness surfaces can be approximated, using standard multiple regression techniques, by

$$\begin{aligned}
S_{qP}(\theta, T_0) &= a_1 - b_1 \cos(4\theta) - c_1 \cos(2\theta), \\
S_{qSV}(\theta, T_0) &= a_2 + b_2 \cos(4\theta), \\
S_{SH}(\theta, T_0) &= a_3 + b_3 \cos(2\theta),
\end{aligned} \tag{C2}$$

[*Bennett*, 1968, 1972]. The difference between the exact and the above approximated slowness surfaces is less than 1%. The coefficients a_i, b_i, and c_i, according to the same authors listed in *Gusmeroli et al.* [2012], are reported in Table 1.

The slowness $S_{\mathrm{iso}}(T)$ in isotropic ice at temperature T may be expressed as

$$S_{\mathrm{iso}}(T) = \frac{10^6}{dT + e} \tag{C3}$$

[*Kohnen*, 1974], with $d = -2.3$ m/°C s and $e = 3795$ m/s for *P* waves and $d = -1.2$ m/°C s and $e = 1915$ m/s for *S* waves.

Acknowledgments
This work was supported by the Italian National Program of Antarctic Research (PNRA–WISSLAKE Project) and the U.S. National Science Foundation (WISSARD Program–NSF 0944794, 0632198, and 0424589). The data for this paper are available by contacting the corresponding author. We thank Mauro Pavan, David S. Heeszel, Jacob I. Walter, Knut Christianson, and Robert W. Jacobel for their contribution in the field. We also thank Marion Bougamont for providing her ice sheet models, which were useful to validate the results of this work. Finally, we thank Olaf Eisen for his useful suggestions, and Marco Peronio for his picking program (SPIC).

References

Abo-Zena, A. (1977), Radiation from a finite cylindrical explosive source, *Geophysics*, *42*(7), 1384–1393.
Acharya, H. K., and C. R. Bentley (1978), Investigations of surface-wave dispersion in an inhomogeneous medium by the finite difference method, *Bull. Seismol. Soc. Am.*, *88*(5), 1381–1386.
Aki, K., and P. G. Richards (2002), *Quantitative Seismology,* 2nd ed., Univ. Science Books, Sausalito, Calif.
Alley, R. B. (1988), Fabrics in polar ice sheets: Development and prediction, *Science*, *240*, 493–495.
Alley, R. B., J. H. Perepezko, and C. R. Bentley (1986a), Grain growth in polar ice: I. Theory, *J. Glaciol.*, *32*, 415–424.
Alley, R. B., J. H. Perepezko, and C. R. Bentley (1986b), Grain growth in polar ice: II. Application, *J. Glaciol.*, *32*, 425–433.
Anandakrishnan, S. (1996), Seismic reflections from an internal layer: Fabric change or moraine?, *Eos Trans. AGU*, *77*(17), Spring Meet. Suppl., Abstract O12B-04.
Anandakrishnan, S. (1999), Strong anisotropy in ice stream C detected by shear-wave splitting, Sixth Annual WAIS Workshop, Sterling, Va.
Anandakrishnan, S., and C. R. Bentley (1993), Micro-earthquakes beneath Ice Streams B and C, West Antarctica: Observations and implications, *J. Glaciol.*, *39*(133), 455–462.
Anandakrishnan, S., J. J. Fitzpatrick, R. B. Alley, A. J. Gow, and D. A. Meese (1994), Shear-wave detection of asymmetric *c*-axis fabrics in the GISP2 ice core, *J. Glaciol.*, *40*(136), 491–496.
Armstrong, M. (2009), Multichannel Analysis of Surface Waves (MASW) determined surface wave velocity profile and its relation to observations of the near surface polar firn layers, *Project Rep., GCAS 11, 2008/09*, Univ. of Canterbury. [Available at http://www.anta.canterbury.ac.nz/courses/gcas/reports/Projects%20GCAS%2011.shtml.]
Auld, B. A. (1990), *Acoustic Fields and Waves in Solids*, vol. 1, Krieger Company, Malabar, Fla.
Backus, G. E. (1962), Long-wave elastic anisotropy produced by horizontal layering, *J. Geophys. Res.*, *67*, 4427–4440.
Bass, R., D. Rossberg, and G. Ziegler (1957), Die elastichen konstanten des eises, *Z. Phys. A*, *149*, 199–203.
Beaty, K. S., D. R. Schmitt, and M. Sacchi (2002), Simulated annealing inversion of multimode Rayleigh wave dispersion curves for geological structure, *Geophys. J. Int.*, *151*, 622–631.
Beem, L. H., K. C. Jezek, and C. J. Van Der Veen (2010), Basal melt rates beneath Whillans Ice Stream, West Antarctica, *J. Glaciol.*, *56*(198), 647–654.
Bennett, H. F. (1968), An investigation into velocity anisotropy through measurements of ultrasonic-wave velocities in snow and ice cores from Greenland and Antarctica, PhD thesis, Univ. of Wisconsin-Madison, Madison, Wis.
Bennett, H. F. (1972), *Measurement of Ultrasonic Wave Velocities in Ice Cores From Greenland and Antarctica*, CRREL Research Report No. 237, Hanover, NH.
Bentley, C. R. (1971), Seismic anisotropy of the West Antarctic Ice Sheet, in *Antarctic Snow and Ice Studies II, Antarctic Research Series*, vol. 16, edited by A. P. Crary, pp. 131–177, AGU, Washington, D. C.
Bentley, C. R. (1987), Antarctic ice streams: A review, *J. Geophys. Res.*, *92*, 8843–8858.
Bentley, C. R., and H. Kohnen (1976), Seismic refraction measurements of internal friction in Antarctic ice, *J. Geophys. Res.*, *81*(8), 1519–1526.
Bindschadler, R. A., M. A. King, R. B. Alley, S. Anandakrishnan, and L. Padman (2003), Tidally controlled stick-slip discharge of a West Antarctic ice stream, *Science*, *301*, 1087–1089.
Blankenship, D. D., and C. R. Bentley (1987), The crystalline fabric of polar ice sheets inferred from seismic anisotropy, in *The Physical Basis of Ice Sheet Modelling, (Proceedings of the Vancouver Symposium, August 1987)*, vol. 170, pp. 17–28, IAHS Press, Institute of Hydrology, Wallingford, Oxfordshire, U. K.
Blankenship, D. D., C. R. Bentley, S. T. Rooney, and R. B. Alley (1986), Seismic measurements reveal a saturated porous layer beneath an active Antarctic ice stream, *Nature*, *322*, 54–57, doi:10.1038/322054a0.
Blankenship, D. D., C. R. Bentley, S. T. Rooney, and R. B. Alley (1987), Till beneath ice stream B. 1. Properties derived from seismic traveltimes, *J. Geophys. Res.*, *92*(B9), 8903–8911.
Bouchez, J. L., and P. Duval (1982), The fabric of polycrystalline ice deformed in simple shear: Experiments in torsion, natural deformation and geometrical interpretation, *Textures Microstruct.*, *5*, 171–190.
Brockamp, B., and H. Querfurth (1965), Untersuchungen über die elastizitaskonstanten von see und kunsteis, *Polarforschung*, *34*, 253–262.
Brown, R. J., D. C. Lawton, and S. P. Cheadle (1991), Scaled physical modelling of anisotropic wave propagation: Multioffset profiles over an orthorhombic medium, *Geophys. J. Int.*, *107*, 693–702.
Budd, W. F., and T. H. Jacka (1989), A review of ice rheology for ice sheet modeling, *Cold Reg. Sci. Technol.*, *16*, 107–104.
Bush, I., and S. Crampin (1987), Observations of EDA and PTL anisotropy in shear-wave VSP, 57th Annual Meeting of Society of Exploration Geophysicists, Mtg. Exp., 646-649, New Orleans, La.
Carcione, J. M. (2015), *Wave Fields in Real Media: Theory and Numerical Simulation of Wave Propagation in Anisotropic, Anelastic, Porous and Electromagnetic Media,* 3rd ed., Elsevier, Amsterdam.
Carcione, J. M., D. Gei, and S. Treitel (2010), The velocity of energy through a dissipative medium, *Geophysics*, *75*(2), T37–T47, doi:10.1190/1.3346064.
Carcione, J. M., S. Picotti, and J. E. Santos (2012), Numerical experiments of fracture-induced velocity and attenuation anisotropy, *Geophys. J. Int.*, *191*, 1179–1191, doi:10.1111/j.1365-246X.2012.05697.x.
Carcione, J. M., B. Gurevich, J. E. Santos, and S. Picotti (2013), Angular and frequency dependent wave velocity and attenuation in fractured porous media, *Pure Appl. Geophys.*, *170*, 1673–1683, doi:10.1007/s00024-012-0636-8.
Cercato, M. (2009), Addressing non-uniqueness in linearized multichannel surface wave inversion, *Geophys. Prospect.*, *57*, 27–47.
Červený, V. (2001), *Seismic Ray Theory*, Cambridge Univ. Press, Cambridge, U. K.
Christianson, K., R. W. Jacobel, H. J. Horgan, S. Anandakrishnan, and R. B. Alley (2012), Subglacial Lake Whillans—Ice-penetrating radar and GPS observations of a shallow active reservoir beneath a West Antarctic ice stream, *Earth Planet. Sci. Lett.*, *331-332*, 237–245.
Christoffersen, P., M. Bougamont, S. P. Carter, H. A. Fricker, and S. M. Tulaczyk (2014), Significant groundwater contribution to Antarctic ice streams hydrologic budget, *Geophys. Res. Lett.*, *41*, 2003–2010, doi:10.1002/2014GL059250.
Crampin, S. (1994), The fracture criticality of crustal rocks, *Geophys. J. Int.*, *118*, 428–438.
Crampin, S. (2011), Shear-wave splitting: New geophysics, and earthquake stress-forecasting, in *Encycl. Solid Earth Geophys.*, vol. 2, edited by H. Gupta, pp. 1355–1362, Springer, Heidelberg, Germany.
Dahl-Jensen, D., and N. S. Gundestrup (1987), Constitutive properties of ice at Dye 3, Greenland, in *The Physical Basis of Ice Sheet*

Modelling, (Proceedings of the Vancouver Symposium, August 1987), vol. 170, pp. 31–43, IAHS Press, Institute of Hydrology, Wallingford, Oxfordshire, U. K.

Dantl, G. (1968), Die elastichn moduln voin eis-einkristallen, *J. Phys. Condens. Matter*, *7*, 390–397.

Diprinzio, C. L., L. A. Wilen, R. B. Alley, J. J. Fitzpatrick, M. K. Spencer, and A. J. Gow (2005), Fabric and texture at Siple Dome, Antarctica, *J. Glaciol.*, *51*(173), 281–290.

Durand, G., A. Svensson, S. Kipfstuhl, A. Persson, O. Gagliardini, F. Gillet, J. Sjolte, M. Montagnat, and D. Dahl-Jensen (2009), Evolution of the texture along the EPICA dome C ice core, in *Low Temperature Science Supplement Issue: Physics of Ice Core Records II*, vol. 68, pp. 91–106, Institute of Low Temperature Science, Hokkaido Univ., Sapporo, Japan.

Engelhardt, H., and W. B. Kamb (1997), Basal hydraulic system of a West Antarctic ice stream: Constraints from borehole observations, *J. Glaciol.*, *43*(144), 207–230.

Engelhardt, H., and W. B. Kamb (1998), Basal sliding of Ice Stream B, West Antarctica, *J. Glaciol.*, *44*(147), 223–230.

Fricker, H. A., and T. Scambos (2009), Connected subglacial lake activity on lower Mercer and Whillans Ice Streams, West Antarctica, 2003–2008, *J. Glaciol.*, *55*(190), 303–315.

Fricker, H. A., T. A. Scambos, R. A. Bindschadler, and L. Padman (2007), An active subglacial water system in West Antarctica mapped from space, *Science*, *315*(1544), 1544–1548.

Fricker, H. A., et al. (2011), Siple Coast subglacial aquatic environments: The Whillans Ice Stream Subglacial Access Research Drilling (WISSARD) Project, in *Antarctic Subglacial Aquatic Environments, Geophys. Monogr. Ser.*, vol. 192, edited by M. J. Siegert and M. C. Kennicutt, pp. 199–219, AGU, Washington, D. C.

Fujita, S., H. Maeno, S. Uratsuka, T. Furukawa, S. Mae, Y. Fujii, and O. Watanabe (1999), Nature of radio echo layering in the Antarctic ice sheet detected by a two-frequency experiment, *J. Geophys. Res.*, *104*(B6), 13,013–13,024.

Gabriels, P., R. Snieder, and G. Nolet (1987), In situ measurements of shear wave velocity in sediments with higher-mode Rayleigh waves, *Geophys. Prospect.*, *35*, 187–196.

Gammon, R. H., H. Kiefte, M. J. Clouter, and W. W. Denner (1983), Elastic constants of artificial and natural ice samples by Brillouin spectroscopy, *J. Glaciol.*, *29*(103), 433–460.

Geyer, R. L., and S. T. Martner (1969), SH-waves from explosive sources, *Geophysics*, *34*, 893–905.

Gow, A. J., and D. A. Meese (2007), Physical properties, crystalline textures and *c*-axis fabrics of the Siple Dome (Antarctica) ice core, *J. Glaciol.*, *53*(183), 573–584.

Gow, A. J., and T. Williamson (1976), Rheological implications of the internal structure and crystal fabrics of the West Antarctic ice sheet as revealed by deep core drilling at Byrd Station, *Geol. Soc. Am. Bull.*, *63*(12), 1665–1677.

Gow, A. J., D. A. Meese, R. B. Alley, J. J. Fitzpatrick, S. Anandakrishnan, G. A. Woods, and B. C. Elder (1997), Physical and structural properties of the GISP2 ice cores, *J. Geophys. Res.*, *102*(C12), 26,559–26,576.

Greenhalgh, S. A., and D. W. King (1981), Curved raypath interpretation of seismic refraction data, *Geophys. Prospect.*, *29*(6), 853–882.

Green, R. E., and L. McKinnon (1956), Determination of the elastic constants of ice single crystals by an ultrasonic pulse method, *J. Acoust. Soc. Am.*, *28*, 1292–1292.

Gusmeroli, A., E. C. Pettit, J. H. Kennedy, and C. Ritz (2012), The crystal fabric of ice from full-waveform borehole sonic logging, *J. Geophys. Res.*, *117*, F03021, doi:10.1029/2012JF002343.

Heelan, P. A. (1953a), Radiation from a cylindrical source of finite length, *Geophysics*, *18*, 685–696.

Heelan, P. A. (1953b), On the theory of head waves, *Geophysics*, *18*, 871–893.

Herglotz, G. (1907), Über das Benndorfsche Problem der Fortpflanzungsgeschwindigkeit der Erdbebenstrahlen, Physikal, *Z. Geophys.*, *8*, 145–147.

Herrmann, R. B. (2013), Computer programs in seismology: An evolving tool for instruction and research, *Seismol. Res. Lett.*, *84*, 1081–1088, doi:10.1785/0220110096.

Herron, M. M., and C. C. Langway (1980), Firn densification, an empirical model, *J. Glaciol.*, *25*, 373–385.

Herron, S. L., C. C. Langway, and K. A. Bruegger (1982), Ultrasonic velocities and crystalline anisotropy in the ice core from DYE 3, Greenland, in *Greenland Ice Core: Geophysics, Geochemistry, and the Environment, Geophys. Monogr. Ser.*, vol. 33, edited by C. C. Langway, H. Oeschger, and W. Dansgaard, pp. 23–31, AGU, Washington, D. C.

Hobbs, P. V. (1974), *Ice Physics*, Clarendon Press, Oxford, U. K.

Hofstede, C., O. Eisen, A. Diez, D. Jansen, Y. Kristoffersen, A. Lambrecht, and C. Mayer (2013), Investigating englacial reflections with vibro- and explosive-seismic surveys at Halvfarryggen ice dome, Antarctica, *Ann. Glaciol.*, *54*(64), 189–200, doi:10.3189/2013AoG64A064.

Hooke, R. L. (1973), Structure and flow in the margin of the Barnes Ice Cap, Baffin Island, N. W. T., Canada, *J. Glaciol.*, *12*(66), 423–438.

Horgan, H. J., S. Anandakrishnan, R. B. Alley, L. E. Peters, G. P. Tsoflias, D. E. Voigt, and J. P. Winberry (2008), Complex fabric development revealed by englacial seismic reflectivity: Jakobshavn Isbrae, Greenland, *Geophys. Res. Lett.*, *35*, L10501, doi:10.1029/2008GL033712.

Horgan, H. J., S. Anandakrishnan, R. B. Alley, P. G. Burkett, and L. E. Peters (2011), Englacial seismic reflectivity: Imaging crystal orientation fabric in West Antarctica, *J. Glaciol.*, *57*(204), 639–650.

Horgan, H. J., S. Anandakrishnan, R. W. Jacobel, K. Christianson, R. B. Alley, D. S. Heeszel, S. Picotti, and I. W. Jacob (2012), Subglacial Lake Whillans—Seismic observations of a shallow active reservoir beneath a West Antarctic ice stream, *Earth Planet. Sci. Lett.*, *331-332*, 201–209.

Hörhold, M. W., S. Kipfstuhl, F. Wilhelms, J. Freitag, and A. Frenzel (2011), The densification of layered polar firn, *J. Geophys. Res.*, *116*, F01001, doi:10.1029/2009JF001630.

Jona, F., and P. Scherrer (1952), Die elastischen konstanten von eis einkristallen, *Helv. Phys. Acta*, *25*, 35–54.

Joughin, I., S. Tulaczyk, R. A. Bindschadler, and S. F. Price (2002), Changes in West Antarctic ice stream velocities: Observation and analysis, *J. Geophys. Res.*, *107*(B11), 2289, doi:10.1029/2001JB001029.

Joughin, I., et al. (2005), Continued deceleration of Whillans Ice Stream, West Antarctica, *Geophys. Res. Lett.*, *32*, L22501, doi:10.1029/2005GL024319.

Kamb, B. (2001), Basal zone of the West Antarctic ice streams and its role in the lubrication of their rapid motion, in *The West Antarctic Ice Sheet: Behavior and Environment, Antarctic Research Series*, vol. 77, edited by R. B. Alley and R. A. Bindschadler, pp. 157–200, AGU, Washington, D. C.

King, E. C., and E. P. Jarvis (2007), Use of shear waves to measure Poisson's ratio in polar firn, *J. Environ. Eng. Geophys.*, *12*(1), 15–21.

Kirchner, J. F., and C. R. Bentley (1979), Seismic short refraction studies on the Ross Ice Shelf, Antarctica, *J. Glaciol.*, *24*(90), 313–319.

Kohnen, H. (1972), On the relation between seismic velocities and density in firn and ice, *Z. Geophys.*, *38*, 925–935.

Kohnen, H. (1974), The temperature dependence of seismic waves in ice, *J. Glaciol.*, *13*(67), 144–147.

Kohnen, H., and C. R. Bentley (1973), Seismic refraction and reflection measurements at Byrd Station, Antarctica, *J. Glaciol.*, *12*(64), 101–111.

Lay, T., and T. C. Wallace (1995), *Modern Global Seismology*, Academic Press, San Diego, Calif.

Luke, B., and C. Calderon-Macías (2007), Inversion of seismic surface wave data to resolve complex profiles, *J. Geotech. Geoenviron. Eng.*, *133*, 155–165.
MacAyeal, D. R. (1989), Large-scale ice flow over a viscous basal sediment: Theory and application to ice stream B, Antarctica, *J. Geophys. Res.*, *94*(B4), 4071–4087, doi:10.1029/JB094iB04p04071.
Mainprice, D., and A. Nicolas (1989), Development of shape and lattice preferred orientations: Application to the seismic anisotropy of the lower crust, *J. Struct. Geol.*, *11*(1–2), 175–189.
Martín, C., G. H. Gudmundsson, H. D. Pritchard, and O. Gagliardini (2009), On the effects of anisotropic rheology on ice flow, internal structure, and the age-depth relationship at ice divides, *J. Geophys. Res.*, *114*, F04001, doi:10.1029/2008JF001204.
Matsuoka, K., T. Furukawa, S. Fujita, H. Maeno, S. Uratsuka, R. Naruse, and O. Watanabe (2003), Crystal orientation fabrics within the Antarctic ice sheet revealed by a multipolarization plane and dual-frequency radar survey, *J. Geophys. Res.*, *108*(B10), 2499, doi:10.1029/2003JB002425.
Matsuoka, K., L. Wilen, S. P. Hurley, and C. F. Raymond (2009), Effects of birefringence within ice sheets on obliquely propagating radio waves, *IEEE Trans. Geosci. Remote Sens.*, *47*(5), 1429–1443, doi:10.1109/TGRS.2008.2005201.
McMechan, G. A., and M. J. Yedlin (1981), Analysis of dispersive waves by wave field transformation, *Geophysics*, *46*, 869–874.
Nolet, G. (1981), Linearized inversion of (teleseismic) data, in *The Solution of the Inverse Problem in Geophysical Interpretation*, edited by R. Cassinis, pp. 9–37, Plenum Press, New York.
Nowack, R. L. (1990), Tomography and the Herglotz-Wiechert inverse formulation, *Pure Appl. Geophys.*, *133*, 305–315.
Parker, R. L. (1994), *Geophysical Inverse Theory*, Princeton Univ. Press, Princeton, N. J.
Pattyn, F. (2000), Ice-sheet modelling at different spatial resolutions: Focus on the grounding zone, *Ann. Glaciol.*, *31*(1), 211–216.
Pettit, E. C., T. Thorsteinsson, H. P. Jacobson, and E. D. Waddington (2007), The role of crystal fabric in flow near an ice divide, *J. Glaciol.*, *53*(181), 277–288.
Pettit, E. C., E. D. Waddington, W. D. Harrison, T. Thorsteinsson, D. Elsberg, J. Morack, and M. A. Zumberge (2011), The crossover stress, anisotropy and ice flow law at Siple Dome, West Antarctica, *J. Glaciol.*, *57*(201), 39–52.
Picotti, S., J. M. Carcione, J. E. Santos, and D. Gei (2010), Q-anisotropy in finely-layered media, *Geophys. Res. Lett.*, *37*, L06302, doi:10.1029/2009GL042046.
Picotti, S., J. M. Carcione, and J. E. Santos (2012), Oscillatory numerical experiments in finely layered anisotropic viscoelastic media, *Comput. Geosci.*, *43*, 83–89, doi:10.1016/j.cageo.2012.02.026.
Postma, G. W. (1955), Wave propagation in a stratified medium, *Geophysics*, *20*, 780–806.
Richart, F. E., Jr., J. Hall Jr., and R. D. Woods (1970), *Vibrations of Soils and Foundations*, Prentice-Hall, Engewood Cliffs, N. J.
Röthlisberger, H. (1972), *Seismic Exploration in Cold Regions*, Cold Regions Sci. Eng. Monogr. II-A2a, U. S. Army Cold Regions Res. and Eng. Lab., Hanover, N. H.
Russell-Head, D. S., and W. F. Budd (1979), Ice-sheet flow properties derived from bore-hole shear measurements combined with ice-core studies, *J. Glaciol.*, *24*(90), 117–130.
Santos, J. E., S. Picotti, and J. M. Carcione (2012), Evaluation of the stiffness tensor of a fractured medium with harmonic experiments, *Comput. Meth. Appl. Mech. Eng.*, *247-248*, 130–145, doi:10.1016/j.cma.2012.08.004.
Savage, M. K. (1999), Seismic anisotropy and mantle deformation: What have we learned from shear-wave splitting?, *Rev. Geophys.*, *37*, 65–106.
Sidler, R., J. M. Carcione, and K. Holliger (2008), On the evaluation of the plane-wave reflection coefficients in anelastic media, *Geophys. J. Int.*, *175*, 94–102.
Slack, R. D., D. A. Ebrom, J. A. McDonald, and R. H. Tatham (1993), Thin layers and shear-wave splitting, *Geophysics*, *58*, 1468–1480.
Stevens, J. L., H. Xu, and G. E. Baker (2008), *Analysis of Shear Wave Generation by Decoupled and Partially Coupled Explosions*, vol. 1, pp. 693–703, Orlando, Fla.
Thomsen, L. (1986), Weak elastic anisotropy, *Geophysics*, *51*, 1954–1966.
Thorsteinsson, T., J. Kipfstuhl, and H. Miller (1997), Textures and fabrics in the GRIP ice core, *J. Geophys. Res.*, *102*(C12), 583–599.
Tsoflias, G. P., J. Ivanov, S. Anandakrishnan, H. J. Horgan, L. Peters, D. Voigt, and P. Winberry (2008), Firn and shallow ice profiling at Jakobshavn Glacier using dispersed seismic surface waves, *Eos Trans. AGU*, *89*(53), Fall Meet. Suppl., C11D-0528.
Tulaczyk, S., W. B. Kamb, and H. F. Engelhardt (2000), Basal mechanics of Ice Stream B, West Antarctica: 2. Undrained plastic bed model, *J. Geophys. Res.*, *105*(B1), 483–494, doi:10.1029/1999JB900328.
Tulaczyk, S., et al. (2014), WISSARD at Subglacial Lake Whillans, West Antarctica: Scientific operations and initial observations, *Ann. Glaciol.*, *55*(65), 51–58.
van der Veen, C. J., and I. M. Whillans (1994), Development of fabric in ice, *J. Cold Reg. Sci. Technol.*, *22*, 171–195.
Voigt, D. E., L. E. Peters, and S. Anandakrishnan (2013), "Georods": The development of a four-element geophone for improved seismic imaging of glaciers and ice sheets, *Ann. Glaciol.*, *54*(64), 142–148.
Wathelet, M., D. Jongsman, and M. Ornberger (2004), Surface-wave inversion using a direct search algorithm and its application to ambient vibration measurements, *Near Surf. Geophys.*, *2*, 211–221.
Wiechert, E. (1910), Bestimmung des weges von erdbebenwellen. I. Theoretisches, *Phys. Z.*, *11*, 294–304.
Wiggins, R. A. (1972), The general linear inverse problem: Implication of surface waves and free oscillations for Earth structure, *Rev. Geophys. Space Phys.*, *110*, 251–285.
Wilkinson, D. S. (1988), A pressure-sintering model for the densification of polar firn and glacier ice, *J. Glaciol.*, *34*, 40–45.
Wilson, C. J. L., D. S. Russell-Head, and H. M. Sim (2003), The application of an automated fabric analyzer system to the textural evolution of folded ice layers in shear zones, *Ann. Glaciol.*, *27*(1), 7–17.
Winberry, J. P., S. Anandakrishnan, R. B. Alley, R. A. Bindschadler, and M. A. King (2009), Basal mechanics of ice streams: Insights from the stick-slip motion of Whillans Ice Stream, West Antarctica, *J. Geophys. Res.*, *114*, F01016, doi:10.1029/2008JF001035.
Winberry, J. P., S. Anandakrishnan, R. B. Alley, A. W. Douglas, and J. P. Martin (2014), Tidal pacing, skipped slips and the slowdown of Whillans Ice Stream, Antarctica, *J. Glaciol.*, *60*(222), 795–807, doi:10.3189/2014JoG14J038.
Wittlinger, G., and V. Farra (2012), Observation of low shear wave velocity at the base of the polar ice sheets: Evidence for enhanced anisotropy, *Geophys. J. Int.*, *190*(1), 391–405.
Woodruff, A. H., and C. S. M. Doake (1979), Depolarization of radio waves can distinguish between floating and grounded ice sheets, *J. Glaciol.*, *23*, 223–232.
Yamanaka, H. (2005), Comparison of the performance of heuristic search methods for phase velocity inversion in the shallow surface wave method, *J. Environ. Eng. Geophys.*, *10*, 163–173.
Xia, J., R. D. Miller, and C. B. Park (1999), Estimation of near-surface shear wave velocity by inversion of Rayleigh waves, *Geophysics*, *64*, 691–700.
Zhang, S. X., Y. Wang, H. Zhou, and L. S. Chan (2009), Dispersion splitting of Rayleigh waves in layered azimuthally anisotropic media, *J. Appl. Geophys.*, *67*, 130–142.